Laser Powder Bed Fusion of Ultrahigh Strength Steel AerMet 100

Department of Mining and Materials Engineering

McGill University

Montreal, Quebec, Canada

November 2018

A thesis submitted to McGill University in partial fulfillment of the requirements of the degree of Master of Engineering in the Department of Mining and Materials Engineering

Abstract

Laser powder bed fusion(LPBF) is one of the additive manufacturing processes which uses a laser as a heat source and fabricates components from metallic powders. In this study, a custom-built pulsed laser powder bed fusion (PLPBF) system was used to fabricate a series of ultra-high strength steel AerMet 100 specimens for materials characterization and mechanical property evaluation.

The initial phase of the research aims to study the feasibility of additive manufacturing of AerMet 100. Crack-free specimens were successfully fabricated through a custom-built pulsed LPBF system. Two post-PLPBF heat treatments, stress relief and three-step heat treatment, were applied to the AM fabricated specimens for microstructure evolution study. The microstructure of build-up, heat affected zone (HAZ) and substrate with respect to as-deposited, stress-relieved and heat-treated samples was characterized using scanning electron microscopy (SEM), Energy-dispersive X-ray spectroscopy (EDS), and X-ray diffraction (XRD). The XRD results indicated that the predominant phases of build-up area in the as-deposited condition are martensite and retained austenite. The hardness results showed a similar or superior hardness of post heat-treated samples to a wrought heat-treated AerMet 100 (606HV). The existence of Cr-rich M23C6 carbides in the stress-relieved sample were detected by XRD; their presence strengthened the martensite matrix, which resulted in an increased hardness. The elimination of retained austenite and homogenized martensitic structure in the heat-treated sample improved the hardness.

Résumé

La fusion par laser sur lit de poudre (LPBF, en anglais) est un des procédés de fabrication additive qui utilise un laser comme source de chaleur et fabrique des composants à partir de poudres métalliques. Dans cette étude, un système de fusion au laser pulsé sur lit de poudre (PLPBF, en anglais) fabriqué sur mesure a été utilisé pour concevoir une série d'échantillons d'acier ultra-haute résistance AerMet 100 destinés à la caractérisation des matériaux et à l'évaluation des propriétés mécaniques.

La phase initiale de la recherche vise à étudier la faisabilité de la fabrication additive d'AerMet 100. Des spécimens sans fissure ont été fabriqués avec succès grâce au système LPBF pulsé sur mesure. Deux traitements thermiques post-PLPBF, un traitement de relaxation des contraintes et un traitement thermique en trois étapes, ont été appliqués aux échantillons conçus par fabrication additive (AM, en anglais) pour l'étude de l'évolution de la microstructure. La microstructure des zones accumulées, affectées thermiquement (HAZ, en anglais) et du substrat par rapport aux échantillons tel que déposés, libérés de stress et soumis à un traitement thermique a été caractérisée par microscopie électronique à balayage (SEM, en anglais), spectroscopie de rayons X à dispersion d'énergie (EDS, en anglais) et diffraction des rayons X (XRD, en anglais). Les résultats de la XRD ont indiqué que les phases prédominantes de la zone d'accumulation à l'état tel que déposé sont la martensite et l'austénite. Les résultats de dureté des échantillons post-traités thermiquement montrent une dureté similaire ou supérieure à un échantillon brut d'AerMet 100 (606HV) traité thermiquement. L'existence de carbures $M_{23}C_6$ riches en Cr dans l'échantillon libéré de stress a été détectée par XRD; leur présence a renforcé la matrice de martensite ce qui a entraîné une augmentation de la dureté. L'élimination de l'austénite et la structure martensitique homogénéisée dans l'échantillon traité thermiquement a amélioré la dureté.

Acknowledgements

It is an amazing experience for me for the past two years of hardships, difficulties as well as enjoyment and success. And now I am approaching the finish line of my journey in pursuing a master's degree. Looking back my whole master's career, I have met so many people who have not only aided me from the work but we also have shared so many precious moments together.

Foremost, I would like to express my sincere gratitude to my supervisor Prof. Mathieu Brochu for providing me such an opportunity to work in the field of additive manufacturing. It is not only his continuous support of my Master study and research, but also his patience, motivation, enthusiasm, and immense knowledge has enlightened me throughout my entire master's career and kept me on the right track. His guidance helped me in all the time of research and writing of this thesis. I could not have imagined having a better advisor and mentor for my Master study.

I would like to thank all my fellow colleagues McGill Processing and Additive Manufacturing of Advanced Materials (P2AM2) Laboratory. It is such an honor to work in a friendly and innovative group and I am grateful to be a member of it. I would like to give my special thank to Dr. Yaoyao Ding who introduced the entire group to me and always being informative throughout my master's study. I would also like to thank Xianglong Wang for his selfless spirit in helping me with printing the samples and providing technical advice. I would also like to thank Dr. Jose Alberto Muñiz Lerma, Dr. Philippe Hendrickx, Dr. Amy Nommeots-Nomm, Dr. Pierre Hudon, Dany Rasmussen, Abhi Ghosh, Fanny Chainiau and Oscar Sanchez Mata for their kind help during my study. In particular, I am grateful to Dr. Yuan Tian for enlightening me the first glance of research.

I would like to thank my parents, Youjiang Chen and Lijun Li, and all the relatives for providing me with unconditional support. Sincere thanks to my beautiful and lovely girlfriend Qisheng He who has always trusted and supported me.

Last but not the least, I would like to thank all the partners and sponsors McGill University, Centrale Nantes, The University of Sheffield, University of Ottawa, Heroux Devteck, Pratt & Whitney Canada, Digital Product Simulation, Liburdi and GKN Aerospace for their financial and technical supports of this project.

Foreword & Contribution of Authors

This thesis has been written in a manuscript-based format and the manuscript have been presented as Chapter 4, titled:

- *Pulsed Laser Powder Bed Fusion of AerMet 100*

Mr. Mingyang Chen was the primary author for the manuscripts and conducted all the experiments, data collections, material characterizations, analysis and calculations presented. **Professor Mathieu Brochu** supervised the entire project and was the corresponding authors in the manuscript for providing technical advice, guidance, access to equipment necessary to complete the experiments, and funding required for the project. **Dr. Yaoyao Ding** was co-author of the manuscript for assisting in material characterization work and chemical composition analyses of the specimens. **Mr. Xianglong Wang** was co-author of the manuscript for providing technical assistance laser additive manufacturing.

Table of Contents

List of Figures

List of Tables

Chapter 1: Introduction

1.1 Motivation and Objective

Additive Manufacturing (AM) has many different names such as three-dimensional (3D) printing, rapid prototyping (RP), layered manufacturing (LM), and solid freeform fabrication (SFF) etc. According to ASTM standard F2792[1.1], AM is “a process of joining materials to make objects from 3D model data, usually layer upon layer, as opposed to subtractive manufacturing methodology”. In this process, multiple layers are built one on top of the other in the X-Y direction and generating in Z direction. The major attraction of AM is that digital designing and computer-aided design (CAD) have given researchers the ability to make, fix, change and iterate designs through their own willing. With AM, those designs can be made and tested from almost anywhere with short production time[1.2]. AM has some other advantages over conventional fabrication process such as design freedom, no tooling, less materials utilization, versatility and part optimisation. Based on the categorization of technologies into groups where processes using a common type of machine architecture and similar materials transformation physics, AM processes are divided into seven primary families: Binder jetting, Directed energy deposition, Material extrusion, Material jetting, Powder bed fusion, Sheet lamination and Vat photopolymerization[1.3].

Powder bed fusion (PBF) process is one of the first commercialized AM processes. All PBF processes share a common set of characteristics. These include one or multiple thermal sources for inducing fusion between powder particles, a method of controlling powder fusion to a designated area and mechanisms for adding and smoothing powder layers[1.3]. The most common thermal sources for PBF are lasers. Laser powder bed fusion (LPBF) is a subcategory of the PBF family. It is an AM process which can fabricate parts by melting or fusing metallic powders through high-power laser source. LPBF provides lots of advantages such as high materials usage efficiency, a wide range of choice for powder materials, high materials buy-to-fly ratio, intricate geometry fabrication and multi-part assemblies which allows production of multiple parts simultaneously. Based upon these advantages, LPBF process becomes one of the most ideal candidates for fabricating metallic complex components in the industries, especially in aerospace sector. Since the LPBF process is highly parameter sensitive, these parameters, for instance, layer thickness(t), laser power (P), laser scanning speed (v) and scanning path strategy, hatching space(h), laser spot size (d), particle size and distribution, platform pre-heating temperature and laser beam scanning strategy[1.4], will be discussed in detail in Chapter 2.

While significant attention is being directed towards fabricating new components, there is an increasing demand of restoring worn/damaged parts to their original shape and their original design integrity. AM provides a significant cost benefit outcomes specifically in the replacement of structure to an acceptable level of functionality and structural integrity[1.5]. One of the attractions for applying AM to repair aircraft landing gear and extend its life cycle. Landing gear is the undercarriage of an aircraft. It supports the craft when it is not flying, allowing it to take off, land and taxi without damage. It is expected to be strong, tough and offer a good resistance to stress corrosion. AerMet 100 alloy is an ultra-high strength steel for aerospace structural applications which require a combination of high strength, high fracture toughness and good resistance to stress corrosion cracking. It has been used in multiple location in the landing gear system. High content of nickel, chromium and cobalt existing in this alloy makes it a potential candidate for AM repair. This project aims to study the use of AM of AerMet 100 and evaluate its impact on the microstructure and mechanical behavior through heat treatment by comparing the microstructures and mechanical properties of AM fabricated parts with those of conventionally fabricated parts. This study can be later referred to the AM repair of landing gear components.

1.2 Reference

1.1 ASTM-F2792-12a, *Standard Terminology for Additive Manufacturing Technologies*. 2012, ASTM International: West Conshohocken, PA.

1.2 Bandyopadhyay, A. and S. Bose, *Additive manufacturing.* 2016.

1.3 Gibson, I., D.W. Rosen, and B. Stucker, *Additive manufacturing technologies : rapid prototyping to direct digital manufacturing.* 2010.

1.4 Sun, S., M. Brandt, and M. Easton, *2 - Powder bed fusion processes: An overview*, in *Laser Additive Manufacturing*. 2017, Woodhead Publishing. p. 55-77.

1.5 Matthews, N., *Chapter Fifteen - Additive Metal Technologies for Aerospace Sustainment*, in *Aircraft Sustainment and Repair*. 2018, Butterworth-Heinemann: Boston. p. 845-862.

Chapter 2: Literature Review

2.1 AerMet 100

Although the materials selection pool for LPBF is wide, most researches in the recent years are focused on Titanium alloys, Nickel-base superalloy, Cobalt-base superalloy and Aluminum alloys [2.1-2.3]. Comprehensive research on steel is lacking in the AM field. Steel is an alloy mostly consisting of iron and carbon and most carbon steels contain up to 1.5% C, while cast irons normally contain 2 to 4% C. Alloying elements in steel act as the hardening agents and help in preventing dislocations in the iron lattice [2.4].

AerMet 100 is an ultra-high strength steel with a combination of high strength, high fracture toughness and good resistance to stress corrosion cracking which are required for aerospace structural applications such as landing gear component [2.5]. It is produced in wrought form by Carpenter Technology Corporation through vacuum-induction melting (VIM) and vacuum-arc remelting (VAR) to ensure the very low impurity levels necessary to achieve the property specifications with a nominal composition is 0.23% C, 3.1% Cr, 11.1% Ni, 1.2% Mo, 13.4% Co and balance Fe [2.6].

VIM works as an effective degassing of the melt and precise adjustment of the alloy composition. This process is indispensable to produce high purity metal tending to react with oxygen. VIM limits the formation of non-metallic oxides that could result in premature failure of the material. It also provides an extremely low gas content and avoids oxidation of alloy elements [2.7]. The advantages of VIM include an extremely precise adjustment of the alloy composition, melt homogenization and easy removal of the impurities.

VAR is a secondary refining process aiming to improve the cleanliness and refine the structure of VIM ingots. The local solidification rate and the temperature gradient at the liquid solid interface are controlled in this process to achieve a directed dendritic primary structure. This avoids macro segregation and reduces micro segregation of alloy elements during the process[2.7, 2.8]. VAR steels are widely used in application where cleanliness, improved ductility and fracture toughness are essential. The advantages of VAR include removal of dissolved gases, reduction of undesired trace elements and improvement of cleanliness[2.8].

AerMet 100 has a range of alloying additions, their role in the materials behavior will now be discussed. The addition of Molybdenum is to form carbide and help to increase peak hardness [2.9]. Chromium additions form alloy carbides with Molybdenum. The addition of Chromium is to shift the secondary hardening peak to lower temperature during tempering and to higher the hardness value [2.9]. The addition of Cobalt has three main effects [2.10]: (1) Increasing the martensite start temperature (M_s), (2) increasing the activity coefficient of carbide resulting in enhanced diffusion, (3) increasing solid solution strengthening effect. The addition of Nickel increases the weldability of AerMet 100 [2.11] and reduce the peak hardness temperature to a lower temperature. The nickel causes the cementite to destabilize, resulting in the formation of the fine carbides at lower temperature [2.12]. As reported by, R. Ayer and P. Machmeier [2.10], relatively fine and undissolved carbides, (CrTiFeMo)C or MC (where M stands for an appropriate metallic element) and $(CrFeMo)_{23}C_6$ or $M_{23}C_6$, are dispersed in the martensitic matrix in the as-quenched condition.

AerMet 100 is a secondary hardening steel. Secondary hardening steel is a type of quenched and tempered martensitic steel that obtain superior hardness from carbide precipitation during tempering at 450°C and above [2.13]. Above 450°C, one to several percent of a strong carbide-forming alloying elements such as Mo, V, W or Cr becomes significant. During tempering, Cementite (Fe_3C or M_3C) dissolves, making a concession to precipitation and growth of finer M_2C-type carbides [2.9, 2.12, 2.13]. The ability of alloy carbides to increase hardness corresponds to the volume fraction of carbides and the fineness of the alloy carbide dispersion i.e. M_2C carbides are an order of magnitude smaller than M_3C carbides [2.9]. The ultra-high strength and hardness of AerMet 100 is achieved by rapid cooling (quenching) from the austenite phase to form martensite and then tempering to precipitate M_2C carbides which impede dislocation motion. M_2C carbides also help improve fracture toughness because they precipitate at the expense of M_3C carbides that reduce fracture energy by embrittling grain boundaries [2.9, 2.14, 2.15].

The typical microstructure of AerMet 100 is shown in Figure 2.1[2.16]. It mainly consists of lath martensite with a small amount of austenite at the prior austenite grain boundaries. Fine prior austenite grain size in AerMet 100 gives a high resistance to cleavage fracture [2.17].

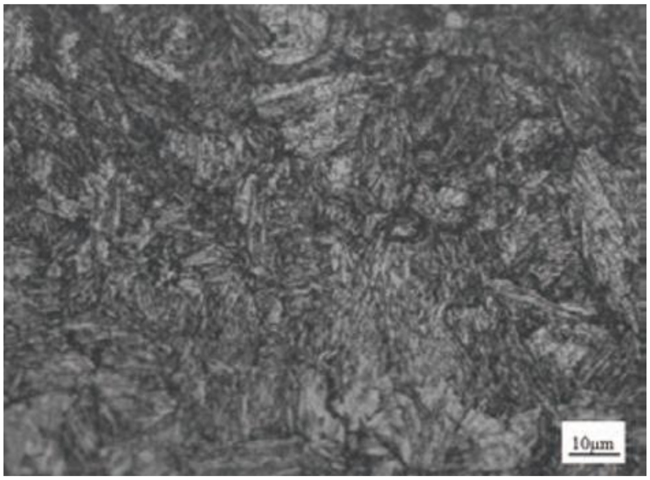

Figure 2.1 Original microstructure of AerMet 100; extracted from reference [2.16]

Heat treatment is usually applied to the wrought AerMet 100 to provide optimized combination of strength and toughness. The recommended heat treatment for AerMet 100 is as follows[2.6]:

1) a solution heat treatment at a temperature of 885 °C for one hour followed by fan cooling.
2) a cryogenic treatment at -73 °C for one hour followed by warming to room temperature in air.
3) an aging treatment at 482 °C for five hours followed by air cooling.

The purpose of solution heat treatment is to reach above Ac_3 temperature (829.4 °C) causing one or more of the alloying constituents to form a solid solution within the metal. This is followed by a rapid cooling to maintain this structure. The purpose of cryogenic treatment is to transform the retained austenite into martensite. It is reported that under an aging temperature of 482 °C, M_2C is formed and to enhance both strength and fracture toughness of AerMet 100 [2.18].

The weldability of Ni-Co-Cr steels is generally considered to be good [2.19] compared to other ultra-high strength steel because of the relative soft and ductile martensite forming in this alloy[2.11]. Based on the welding behaviors of AerMet 100 reported in the recent studies [2.11, 2.20-2.22], in the as-quenched condition, AerMet 100 is resistance to cold cracking which is often associated with welding of high strength quenched and tempered steels. Therefore, it can be a potential candidate for additive manufacturing.

The standard mechanical property specifications of heat-treated wrought AerMet 100 are 1965 MPa ultimate tensile strength (UTS), 1724 MPa yield strength (YS), and 126 MPa$\sqrt{m}$ fracture toughness (K_{IC}) [2.6]. It is found to be equal or superior to the wrought properties of the ultrahigh strength steel Marage 250, 300M, H11, and 4340 [2.23]. As AerMet 100 has high toughness, hardness and can withstand impact loads. It can be used in applications such as armor, fasteners as well as landing gear and jet engine shafts in the aerospace industry.

2.2 Additive Manufacturing (AM) Overview: Laser Powder Bed Fusion (LPBF) Process

Additive Manufacturing (AM) is a general term where material is added to form a desired solid geometry instead of subtracted, as in conventional manufacturing processes, such as machining. The basic principle of AM technology is that the components can be directly fabricated by using a three-dimensional Computer-Aided Design (3D CAD) without the need for process planning [2.24]. Parts are produced by material in layers and each layer is a thin cross-section of the part derived from the original CAD data. The general eight steps of AM process are illustrated in Figure 2.2 [2.24].

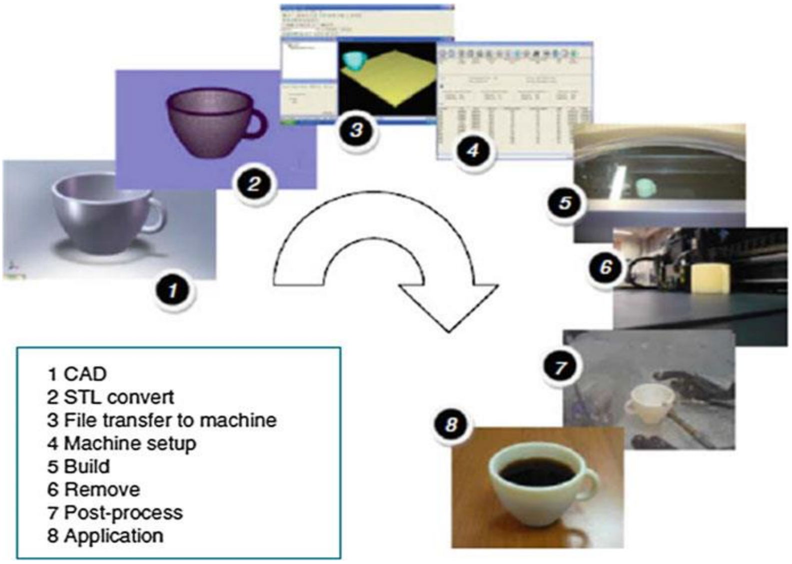

Figure 2.2 General 8 steps of AM process; extracted from reference [2.24]

The Selective Laser Sintering (SLS) process is one of the earliest AM process developed in 1980s at the University of Texas at Austin, USA [2.24]. In 1999, Laser Powder Bed Fusion (LPBF) or Selective Laser Melting (SLM) was developed. SLS is a subcategory of PBF process, which is applied to produce components from powdered materials. In this process, the laser source selectively fuses or melts the powder particles under a protective environment. The raster scanning strategy is utilised in a layer-by-layer approach, permitting building in the Z-direction [2.25]. LPBF is an advanced version of SLS process, where full melting of the powder particles takes place in the powder bed by using laser [2.26, 2.27]. As illustrated in Figure 2.3, the whole process occurs in an protective environment. Powder is spread across the substrate plate to form a thin layer. Then laser is passed through a beam scanner and selectively melts metal powder located within a powder bed on a substrate plate. When the previous layer laser scanning has finished, a new layer of powder will spread again across the build plate. Powder spreading and laser scanning keeps repeating until the whole object is fabricated. Each layer of powder is supplied from a powder storage system via a roller [2.25].

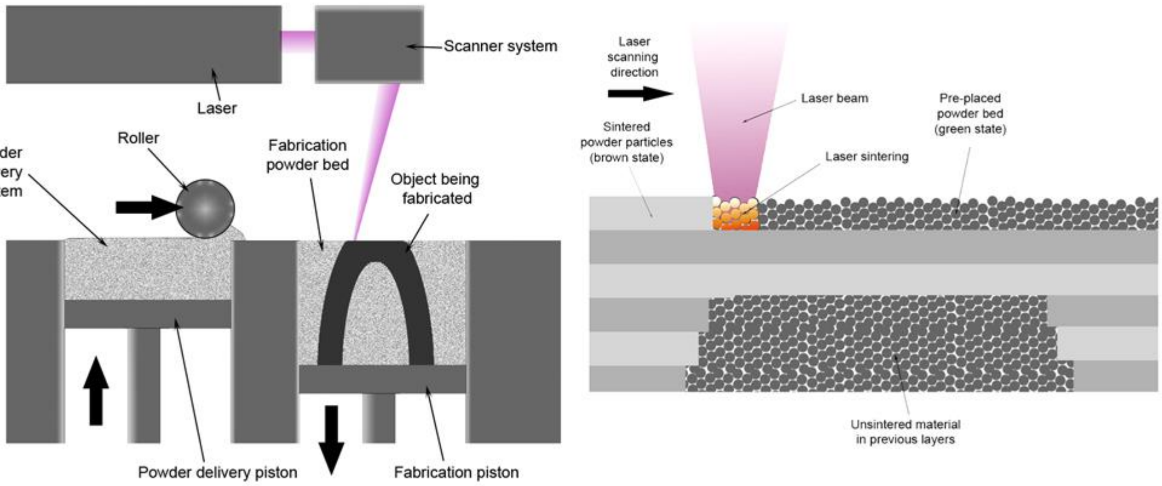

Figure 2.3 Schematics of Laser Powder bed Fuion. Courtesy: Materialgeeza, SLS, Wikipedia

LPBF is one of the most versatile AM processes which can be capable of processing metals, alloys, ceramics and metal matrix composites (MMCs). Laser based AM processes usually have a complex non-equilibrium physical and chemical metallurgical nature depending on the material and process. As shown in

Table 2-1, based on the different mechanisms of laser-powder interaction and the various metallurgical mechanisms (i.e. partial melting vs. full melting), the prevailing AM technologies for the fabrication of metallic components generally has three basic processes: SLS, LPBF and Direct Energy Deposition (DED) [2.26]. Although sharing the same processing apparatus and procedures with SLS, LPBF has superior advantages of producing potential fully dense components with mechanical properties comparable to those of substrate materials. Another major advantage of LPBF is its high feasibility in processing nonferrous pure metals such as Cu, Ti, Al, etc [2.26, 2.28, 2.29]. According to ASTM F2921-11e3[2.30], DED Binder Jetting is another competitive process for fabrication of metallic components. However, since this study is based on laser system, further details of Binder Jetting will not be discussed.

Table 2-1 Classification of AM processes based on different mechanisms of laser–material interaction [2.26]

Powder melting mechanism	**Process**	**Powder mechanism**	**Material**
Partial melting of powder	SLS	Pre-spreading powder before laser scanning	Multi-component metals/alloy powder, Ex-situ MMCs
Full melting of powder	LPBF	Pre-spreading powder before laser scanning	Pure metal powder, Alloy powder, In-situ and Ex-situ MMCs
	DED	Coaxial powder spreading with simultaneous laser scanning	

2.3 Process parameters optimisation

Four main binding mechanism occurs in the Powder Bed Fusion (PBF) system. According to the study by J.P Kruth *et al.*, they are solid state sintering, chemically induced binding, liquid phase sintering-partial melting and full melting [2.31]. In this study, only full melting binding mechanism is discussed since that high-power laser is utilized as the heat source in the LPBF process. Without any post-process densification, high-power laser induces full melting of metallic powder to achieve fully dense parts [2.32]. Thus, to fabricate components with satisfactory properties, process parameters optimization requires to be established. As mentioned by Aboulkhair *et al.*, there are four categories for the overall process parameters which are illustrated in Figure 2.4[2.33].

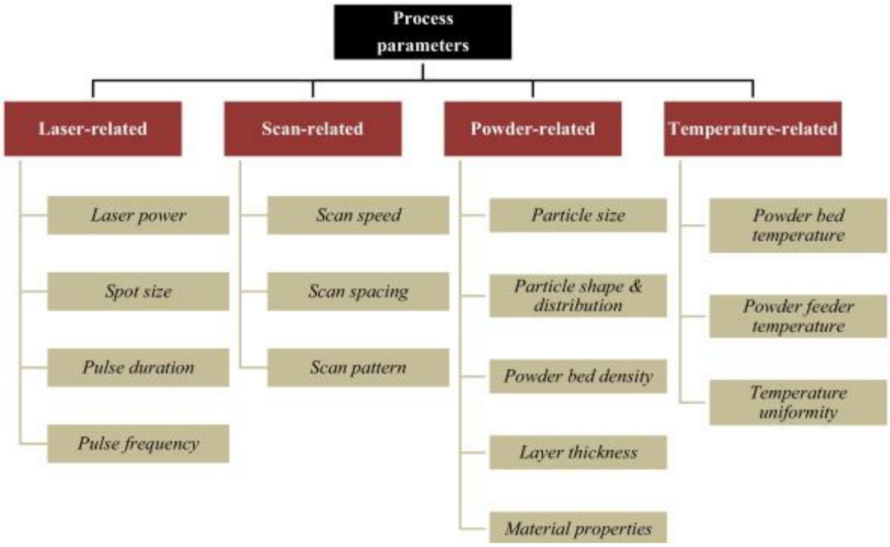

Figure 2.4 Controlling parameters in LPBF process; extracted from reference [2.33]

2.3.1 Powder-related parameters

Powder-related parameters such as powder morphology and particle size distribution (PSD) are the initial step to study. Powder morphology refers to the size, shape, and surface roughness of the powder particles. Powder morphology and PSD have a significant influence on the parameters such as flowability and packing density. Good flowability and high packing density of a powder are highly beneficial in fabricating homogeneous and dense sample which having an influence on the mechanical properties of as-built components. From the previous studies, highly spherical powder particles are often desired in the LPBF process. Particle shapes that conform towards unity tend to enhance powder packing density as well as flowability [2.27, 2.34]. On the other hand, the flowability of non-spherical powder is obstructed because the particles tend to interlock mechanically and entangle with each other. Therefore, spherical powder can improve the overall quality of the fabricated component by reducing porosity, surface roughness and balling effect [2.34-2.36]. Moreover, good powder flowability is also critical in LPBF process. An efficient and uniform powder layer spreading on the previous layer can certainly increase the consolidation performance. In addition, powders with rough surface resulting in increasing inter-particle friction and causing the reduction of powder flowability [2.37].

Study from Simchi *et al*. shows that finer powders (< 50 µm) usually have a better densification since finer particles provide a larger surface area to absorb more laser energy, thereby resulting in an increasing particle melting kinetics [2.38]. However, powder agglomeration and powder flowability decease with reducing particle size. Powder agglomeration also dramatically increases the reflectivity of the powder bed and decreases energy absorption. Besides, powder agglomeration is detrimental to the overall density of the fabricated components [2.38, 2.39]. It is found that the packing density increases if the particle size distribution is extended [2.40]. The maximum packing density occurs when the small particles nearly completely fill the interstices between the larger particles as shown in Figure 2.5. Nevertheless, fine particles will eventually sink into the bottom during powder spreading in the LPBF process instead of filling the gap between coarse powder due to granular convection, known as Brazil-nut effect [2.41].

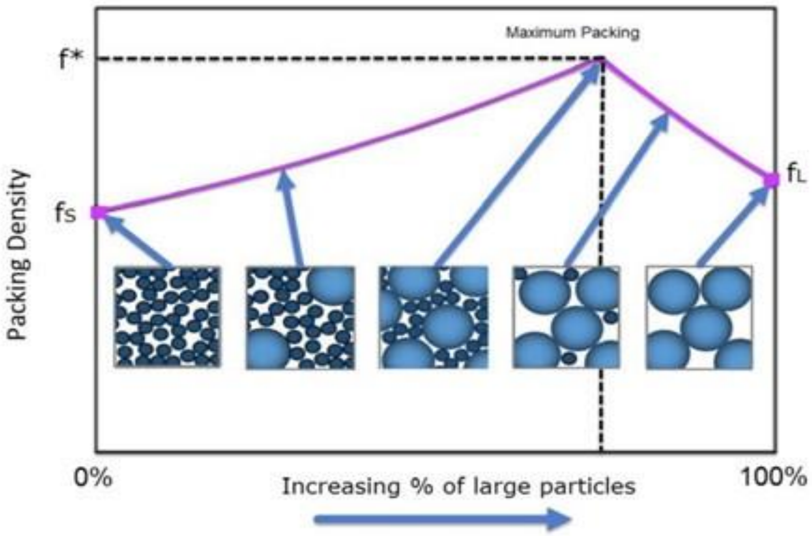

Figure 2.5 Particle size vs. packing density, Courtesy: Additive Manufacturing Magazine

2.3.2 Laser-related parameters

The laser processing variables in LPBF include laser power, laser spot size, pulse duration and pulse frequency. These parameters control the characteristics of the melt pool formed. For example, the maximum melt pool temperature increases dramatically with increasing laser power but slightly decreases with an increasing laser scanning speed [2.42, 2.43]. The temperature gradient in the melt pool increases linearly with an increasing laser power and it is more obvious in materials with low thermal conductivity [2.27, 2.42, 2.44]. There are two major issues associated with laser-related parameters, which are balling and sputtering. Balling is a phenomenon where the molten material does not wet the underlying substrate due to the surface tension and tends to form into a row of independent spheres on the molten track. Balling results in a rougher surface and inherent porosity in the as-built components. It can even jeopardize the powder roller if the size of the balls is large enough to obstruct its movement [2.27, 2.45]. Sputtering is due to melt pool overheating [2.46]. The intensity of the sputter increases with an increasing input energy density [2.47]. Moreover, the sputter formed by melt expulsion is spherical and much larger than the particle size of the feed powder due to agglomeration occurring during sputtering. As shown in the Figure 2.6 [2.47], both balling and sputters effects can remain as defects in the as-built components.

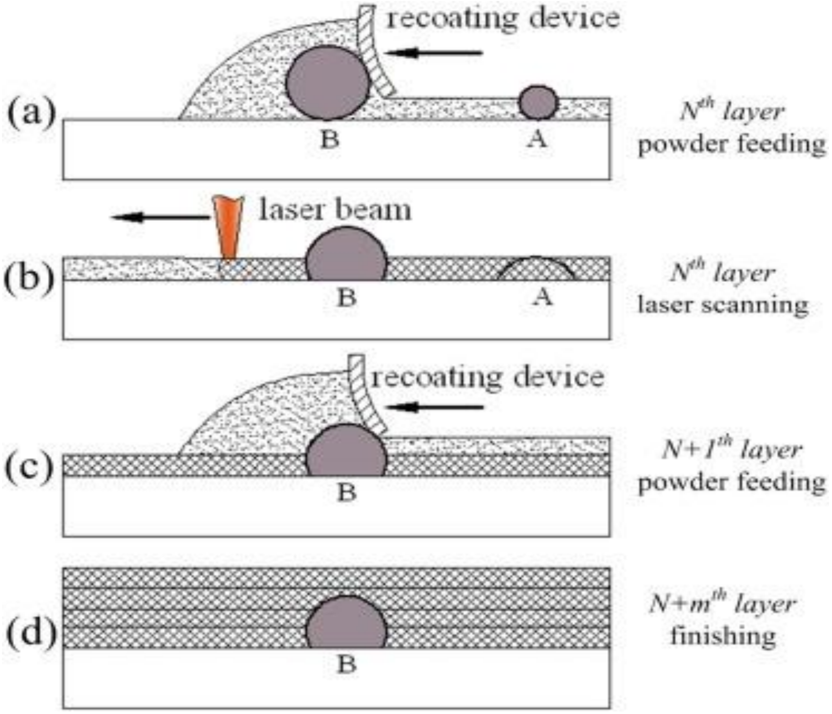

Figure 2.6 Schematic diagrams of the influences of balling and spatter particle (a) N^{th} layer powder feeding, (b) N^{th} layer laser scanning, (c) $N+l^{th}$ layer powder feeding, (d) $N+m^{th}$ layer finishing; extracted from reference [2.47]

2.3.3 Scan-related parameters & Melt pool characterization

The scan-related parameters in the LPBF process include scan speed, scan spacing and scan pattern. For pulse laser system as illustrated in Figure 2.7 [2.48], volumetric energy density (E_p, J/mm^3) can be expressed as:

$$E_p = \frac{P*pd}{l*h*t} \quad (1)$$

Where P is laser power, pd is pulse duration, l is point distance for two consecutive pulse, h is hatching space and t is layer thickness.

For continuous laser system, VED (E_c, J/mm^3) is expressed as [2.27]:

$$E_p = \frac{P}{v*h*t} \quad (2)$$

Where P is laser power, v is laser scanning speed, h is hatching space and t is layer thickness.

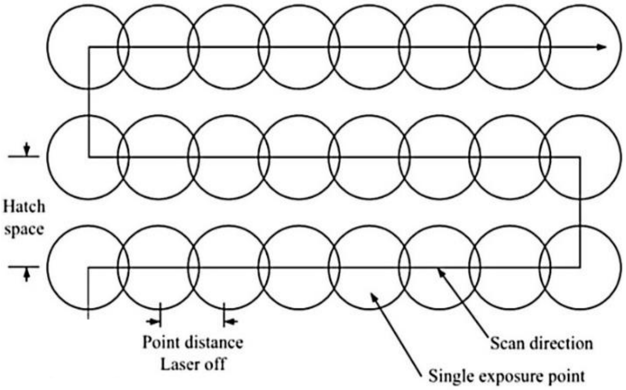

Figure 2.7 Pulse laser system scan pattern; extracted from reference [2.48]

It should be noted that melt pool width decreases and melt pool length increases with an increasing laser scanning speed [2.27]. Spot size has a relative small impact on melt pool dimension compare to the laser powder and scanning speed [2.49].

Powder melting occurs in a localized region of the laser beam, producing small volumes of molten metal, called melt pools. Melt pool morphology and their dimensions are other important factor which can influence the properties of as-built components. Both melt pool morphology and dimensions are determined by the applied laser-related parameters and scan-related parameters The optimised parameters are established by melt pool characterization [2.50]. As depicted in Figure 2.8 (a), Molten pool B has the deepest melt depth and clearly forming keyhole which is inappropriate to the part, but both A and C could be used. Melt pool C would result in greater area coverage, meaning less scan time. As shown in Figure 2.8 (b), it is usual to investigate the surface topography, melt pool length, melt pool depth, melt pool depth angle and melt pool width under different laser parameters during parameter optimisation Increasing laser powder has the predominant effect on melt pool dimension [2.43, 2.44]. Other parameters such as pulse duration, hatching space, layer thickness etc. also have an important impact on melt pool morphology. These parameters can be converted as volumetric energy density (VED).

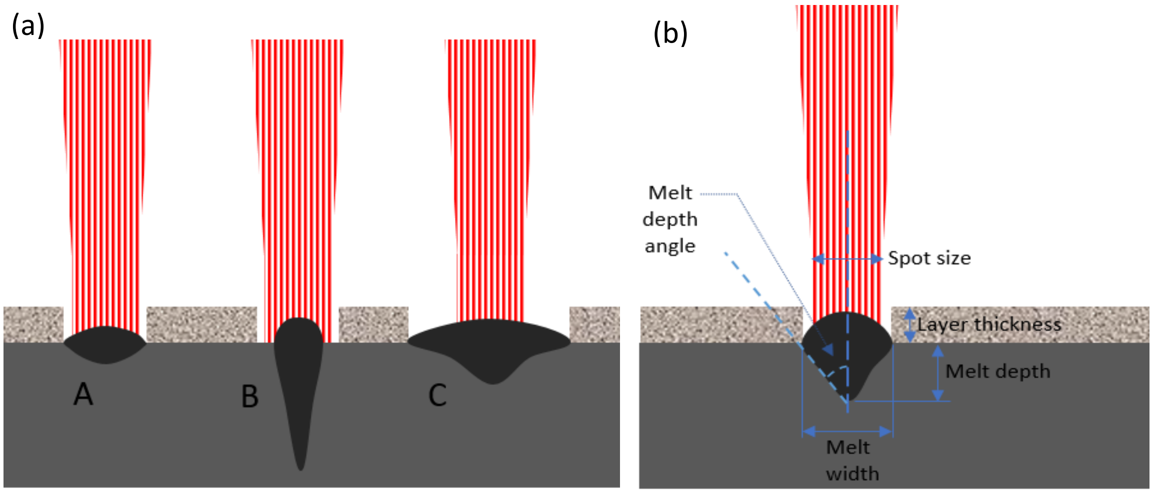

Figure 2.8 (a) Different possible topography, (b) Schematic cross-section through a laser melt pool, Courtesy: Martin McMahon, Linkedin

The research of Gong *et al*. has studied the influence of laser power and scanning speed on the melt pool, which are shown in Figure 2.9 [2.50]. When VED is at a high level, the so-called "keyhole" shape with pores and large melt pool width appeared. This porosity becomes entrapped in as-built components and results in defects. Another effect of high VED is that the large melt pool depth may cause additional melting-solidification history to the previous layer, and a large heat affected zone (HAZ) causing a more complicated phase transformation history to develop[2.50]. Thus, due to the multiple influence of high VED, laser parameters which yield keyhole geometry is not recommended for LPBF process. Low VED causes a reduction of energy penetration and can result in balling as discussed above. Thus, laser parameters of low VED is also not recommended for LPBF process.

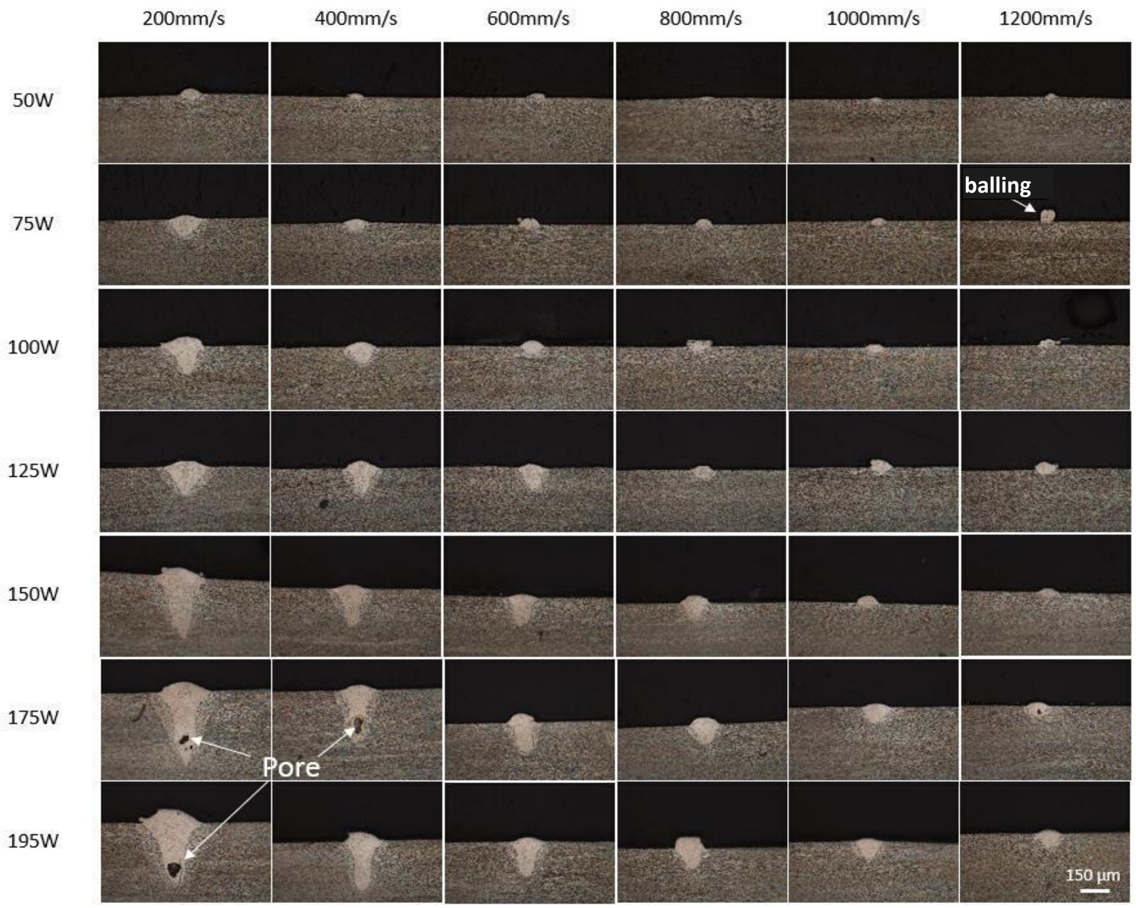

Figure 2.9 Melt pool profile of different laser power and scanning speed; extracted from reference [2.50]

2.4 Solidification and Phase Transformation of AerMet 100 in LPBF process

2.4.1 Solidification in LPBF process

During the solidification of an alloy, there are four basic solidification modes which are planar, cellular, columnar dendritic and equiaxed dendritic [2.51]. It has been observed that the higher the cooling rate, the shorter the solidification time, the finer the microstructure becomes [2.51]. Thus, the cooling rate is the key parameter throughout LPBF process. The effect of the temperature gradient G and the growth rate R dominate the solidification microstructure. As illustrated in Figure 2.10 [2.51], the G/R ratio determines the morphology of solidification structure while the G*R (cooling rate) influences the size of the solidification structure. According to the previous research, the cooling rate generally in PBF process is between 10^5 K/s to 10^7K/s [2.52, 2.53]. Consequently, the microstructure of LPBF fabricated components is much finer than the components fabricated under conventional process with much slower cooling rate such as casting and wrought.

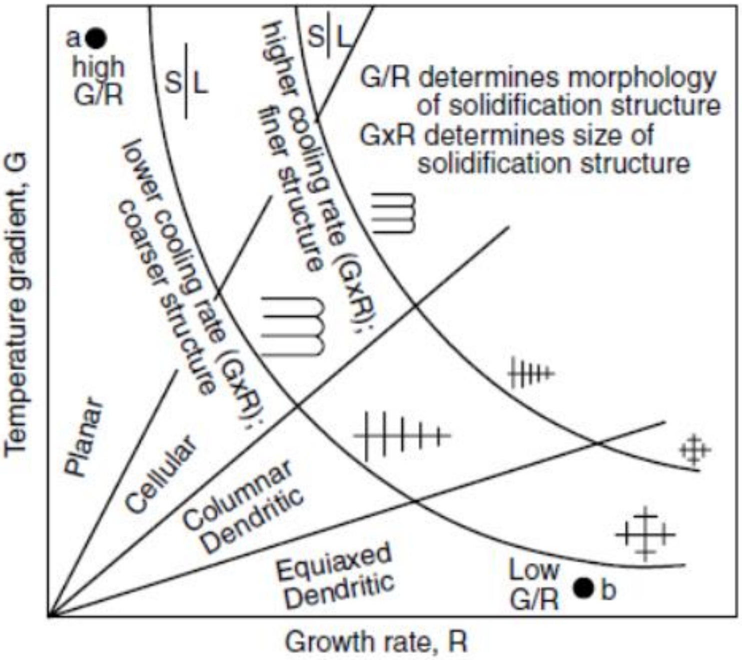

Figure 2.10 Effect of temperature gradient G and growth rate R; extracted from reference [2.51]

2.4.2 Phase Transformation of AerMet 100 in LPBF process

Austenite can transfer into martensite when steel is rapid cooled from temperature above Ac_3 to under Ac_1 [2.54]. According to the studies that performing laser cladding process on AerMet 100[2.22, 2.55], martensitic phase transformation has occurred. Considering the cooling rate of LPBF is similar or superior to laser cladding process [2.52, 2.53, 2.55], martensitic transformation of AerMet 100 also happens during LPBF process. Besides, the temperature range of martensite forming is a function of composition. Almost all alloying elements tend to lower the martensite start temperature (M_s) and martensite finish temperature (M_f)[2.22, 2.56]. For example, one of the predictive equation of martensite start temperature of martensitic stainless steel is [2.56]:

$$M_s(°C) = 540 - (497C + 6.3Mn + 36.3Ni + 10.8Cr + 46.6Mo)$$

In some highly alloyed steels, especially steels containing 4% Ni or more [2.56], the M_f value may be below room temperature. Therefore, some austenite may be retained in the microstructure as shown in Figure 2.11[2.57]. Therefore, further heat treatment may be required to reach the desired mechanical properties.

Figure 2.11 TEM bright-field image of the martensitic microstructure after heat treated at 885°C for 1 h and quenching to room temperature. Retained austenite is present at martensite lath boundaries, as marked by the arrows; extracted from reference [2.57]

2.5 Reference

2.1 Murr, L.E., *et al.*, *Metal Fabrication by Additive Manufacturing Using Laser and Electron Beam Melting Technologies.* Journal of Materials Science & Technology, 2012. **28**(1): p. 1-14.

2.2 Frazier, W.E., *Metal Additive Manufacturing: A Review.* Journal of Materials Engineering and Performance, 2014. **23**(6): p. 1917-1928.

2.3 Bourell, D., *et al.*, *Materials for additive manufacturing.* CIRP Annals, 2017. **66**(2): p. 659-681.

2.4 Campbell, F.C., *Elements of Metallurgy and Engineering Alloys*. 2008, Materials Park, UNITED STATES: A S M International.

2.5 Schmidt, M.L., *AerMet® 100 Alloy for Landing Gear Applications-A Summary of Forging Studies*. 1992, SAE International.

2.6 *AerMet 100 Alloy Technical Datasheet*, C.T. Corporation, Editor. 2011.

2.7 Prasad, N.E. and R.J.H. Wanhill, *Aerospace materials and material technologies. Volume 2, Aerospace material technologies*. 2016, Springer: Singapore.

2.8 Kannan, M., *The Microstructure, Hardness, Impact Toughness, Tensile Deformation and Final Fracture Behavior of four Specialty High Strength Steels*. 2011, University of Akron.

2.9 Graves, J.H., *Effect of Heat Treatment on the Microstructure and Properties of AerMet (trade name) 100 Steel*. 1994, ARMY RESEARCH LAB WATERTOWN MA MATERIALS DIRECTORATE.

2.10 Ayer, R. and P. Machmeier, *Transmission electron microscopy examination of hardening and toughening phenomena in Aermet 100.* Metallurgical and Materials Transactions A, 1993. **24**(9): p. 1943-1955.

2.11 ENGLEHART, D.A., *et al.*, *Fusion Welding of AerMet 100 Alloy*. 1999, ; Sandia National Labs., Albuquerque, NM (US); Sandia National Labs., Livermore, CA (US). p. Medium: P; Size: 63 pages.

2.12 Kwon, H., *et al.*, *Effect of alloying additions on secondary hardening behavior of Mo-containing steels.* Metallurgical and Materials Transactions A, 1997. **28**(3): p. 621-627.

2.13 Shewmon, P.G., *Transformations in metals*. 1969, New York, N.Y.: McGraw-Hill.

2.14 Briant, C.L., *Role of carbides in tempered martensite embrittlement.* Materials Science and Technology, 1989. **5**(2): p. 138-147.

2.15 Grujicic, M., *Design of M2C carbides for coarsening resistance.* Calphad, 1991. **15**(2): p. 179-184.

2.16 Liu, F., *et al.*, *Microstructure and mechanical properties of AerMet 100 ultra-high strength steel joints by laser welding.* Journal of Wuhan University of Technology-Mater. Sci. Ed., 2015. **30**(4): p. 827-830.

2.17 Soto, K., *Improving the toughness of ultrahigh strength steel.* 2002.

2.18 Ayer, R. and P. Machmeier, *On the characteristics of M2C carbides in the peak hardening regime of AerMet 100 steel*. Vol. 29. 1998. 903-905.

2.19 Jenney, C.L., *et al.*, *Welding handbook*. 2001, Miami, FL: American Welding Society.

2.20 Shi, X., *et al.*, *Study on the microstructure and mechanical properties of Aermet 100 steel at the tempering temperature around 482 °C.* Journal of Alloys and Compounds, 2016. **679**: p. 184-190.

2.21 Westrich, C. and C.A. Lawrence Livermore National Lab, *Weldability of AerMet 100*. 1990, United States.

2.22 Liu, J., *et al.*, *Microstructures and tensile properties of laser cladded AerMet100 steel coating on 300M steel.* Journal of Materials Science & Technology, 2018. **34**(4): p. 643-652.

2.23 Novotny, P.M. and T.J. McCaffrey, *An Advanced Alloy for Landing Gear and Aircraft Structural Applications - Aerometr® 100 Alloy*. 1992, SAE International.

2.24 Gibson, I., D.W. Rosen, and B. Stucker, *Additive manufacturing technologies : rapid prototyping to direct digital manufacturing.* 2010.

2.25 Badiru, A.B., V.V. Valencia, and D. Liu, *Additive manufacturing handbook : product development for the Defense industry.* 2017.

2.26 Gu, D.D., *et al.*, *Laser additive manufacturing of metallic components: materials, processes and mechanisms.* International Materials Reviews, 2012. **57**(3): p. 133-164.

2.27 Sun, S., M. Brandt, and M. Easton, *Powder bed fusion processes: An overview*, in *Laser Additive Manufacturing*. 2017, Woodhead Publishing. p. 55-77.

2.28 Xu, W., *et al.*, *Additive manufacturing of strong and ductile Ti–6Al–4V by selective laser melting via in situ martensite decomposition.* Acta Materialia, 2015. **85**: p. 74-84.

2.29 Louvis, E., P. Fox, and C.J. Sutcliffe, *Selective laser melting of aluminium components.* Journal of Materials Processing Technology, 2011. **211**(2): p. 275-284.

2.30 *ASTM F2921-11e3, Standard Terminology for Additive Manufacturing—Coordinate Systems and Test Methodologies (Withdrawn 2013)*. 2013, ASTM International: West Conshohocken, PA.

2.31 J‐P., K., *et al.*, *Binding mechanisms in selective laser sintering and selective laser melting.* Rapid Prototyping Journal, 2005. **11**(1): p. 26-36.

2.32 Kruth, J.P., *et al.*, *Consolidation phenomena in laser and powder-bed based layered manufacturing.* CIRP Annals, 2007. **56**(2): p. 730-759.

2.33 Aboulkhair, N.T., *et al.*, *Reducing porosity in AlSi10Mg parts processed by selective laser melting.* Additive Manufacturing, 2014. **1-4**: p. 77-86.

2.34 Tan, J.H., W.L.E. Wong, and K.W. Dalgarno, *An overview of powder granulometry on feedstock and part performance in the selective laser melting process.* Additive Manufacturing, 2017. **18**: p. 228-255.

2.35 Khairallah, S.A., *et al.*, *Laser powder-bed fusion additive manufacturing: Physics of complex melt flow and formation mechanisms of pores, spatter, and denudation zones.* Acta Materialia, 2016. **108**: p. 36-45.

2.36 Spierings, A.B., N. Herres, and G. Levy, *Influence of the particle size distribution on surface quality and mechanical properties in AM steel parts.* Rapid Prototyping Journal, 2011. **17**(3): p. 195-202.

2.37 German, R.M., *Powder metallurgy and particulate materials processing : the processes, materials, products, properties and applications*. 2005.

2.38 Simchi, A., *The role of particle size on the laser sintering of iron powder.* Metallurgical and Materials Transactions B, 2004. **35**(5): p. 937-948.

2.39 Kizaki, Y., *et al.*, *Phenomenological studies in laser cladding. Part I. Time-resolved measurements of the absorptivity of metal powder.* Japanese journal of applied physics, 1993. **32**(1R): p. 205.

2.40 Sohn, H.Y. and C. Moreland, *The effect of particle size distribution on packing density.* The Canadian Journal of Chemical Engineering, 1968. **46**(3): p. 162-167.

2.41 Möbius, M., *et al.*, *Brazil-nut effect: Size separation of granular particles*. Vol. 414. 2001. 270.

2.42 Li, Y. and D. Gu, *Parametric analysis of thermal behavior during selective laser melting additive manufacturing of aluminum alloy powder.* Materials & Design, 2014. **63**: p. 856-867.

2.43 Li, R., *et al.*, *Effects of processing parameters on the temperature field of selective laser melting metal powder.* Powder Metallurgy and Metal Ceramics, 2009. **48**(3): p. 186-195.

2.44 Pengpeng, Y. and G. Dongdong, *Molten pool behaviour and its physical mechanism during selective laser melting of TiC/AlSi10Mg nanocomposites: simulation and experiments.* Journal of Physics D: Applied Physics, 2015. **48**(3): p. 035303.

2.45 Kruth, J.P., *et al.*, *Selective laser melting of iron-based powder.* Journal of Materials Processing Technology, 2004. **149**(1): p. 616-622.

2.46 Simonelli, M., *et al.*, *A Study on the Laser Spatter and the Oxidation Reactions During Selective Laser Melting of 316L Stainless Steel, Al-Si10-Mg, and Ti-6Al-4V.* Metallurgical and Materials Transactions A, 2015. **46**(9): p. 3842-3851.

2.47 Liu, Y., *et al.*, *Investigation into spatter behavior during selective laser melting of AISI 316L stainless steel powder.* Materials & Design, 2015. **87**: p. 797-806.

2.48 Ding, X., L. Wang, and S. Wang, *Comparison study of numerical analysis for heat transfer and fluid flow under two different laser scan pattern during selective laser melting.* Optik, 2016. **127**(22): p. 10898-10907.

2.49 Ocylok, S., *et al.*, *Correlations of Melt Pool Geometry and Process Parameters During Laser Metal Deposition by Coaxial Process Monitoring.* Physics Procedia, 2014. **56**: p. 228-238.

2.50 Gong, H., *et al. Melt pool characterization for selective laser melting of Ti-6Al-4V pre-alloyed powder*. in *Solid freeform fabrication symposium*. 2014.

2.51 Kou, S., *Welding metallurgy*. 2003: John Wiley & Sons.

2.52 Zhao, C., *et al.*, *Real-time monitoring of laser powder bed fusion process using high-speed X-ray imaging and diffraction.* Scientific Reports, 2017. **7**(1): p. 3602.

2.53 Scipioni Bertoli, U., *et al.*, *In-situ characterization of laser-powder interaction and cooling rates through high-speed imaging of powder bed fusion additive manufacturing.* Materials & Design, 2017. **135**: p. 385-396.

2.54 Pereloma, E. and D.V. Edmonds, *Phase transformations in steels*. Woodhead Publishing in materials. 2012, Cambridge, UK ;: Woodhead Publishing.

2.55 Sun, S.D., *et al.*, *Evaluation of microstructure and fatigue properties in laser cladding repair of ultrahigh strength AerMet® 100 steel.* Journal of Laser Applications, 2015. **27**(S2): p. S29202.

2.56 Lippold, J.C. and D.J. Kotecki, *Welding metallurgy and weldability of stainless steels*. 2005, Hoboken, NJ: John Wiley.

2.57 Gruber, M., *et al.*, *Characterization of the effect of cryogenic treatment on the tempering behavior of a secondary hardening high Co-Ni steel.* IOP Conference Series: Materials Science and Engineering, 2016. **119**(1): p. 012018.

Chapter 3: Instrumentation and Experimental Procedure

This chapter mainly discusses the materials, experimental procedures, specimen fabrication techniques and characterization techniques that were utilized in this research.

3.1 Materials

Gas atomized AerMet 100 powders supplied by Carpenter Technology Corporation (Reading, PA, USA). After determining the feasibility of additive manufacturing of AerMet 100 and producing a crack-free and condensed sample by using a home-made PLPBF system with optimised laser parameters. The microstructure and mechanical properties of the AM built sample and samples with corresponding heat treatments were compared with wrought heat-treated sample.

3.2 Powder Characterization

Powder characterization including apparent density, powder flowability, particle size distribution (PSD), powder morphology and segregation in the powder were applied to AerMet 100 powder. By using a Hall flowmeter funnel following the ASTM standards B212-13 and B213-13 respectively[3.1, 3.2]. The apparent density and flowability of AerMet 100 powder were measured and considered as good quality for additive manufacturing. PSD was measured by a HORIBA LA-920 Laser Particle Size Analyzer. The morphology of the powder was observed by Hitachi SU3500 scanning electron microscope (SEM). The alloy elements were analyzed by Energy-dispersive X-ray spectroscopy (EDS).

3.2.1 Powder apparent density and powder flowability

The apparent density and powder flowability of AerMet 100 were measured using a Hall flowmeter funnel following the ASTM standards B212-13 and B213-13 respectively[3.1, 3.2]. The detailed setup for measurement is shown in Figure 3.1.

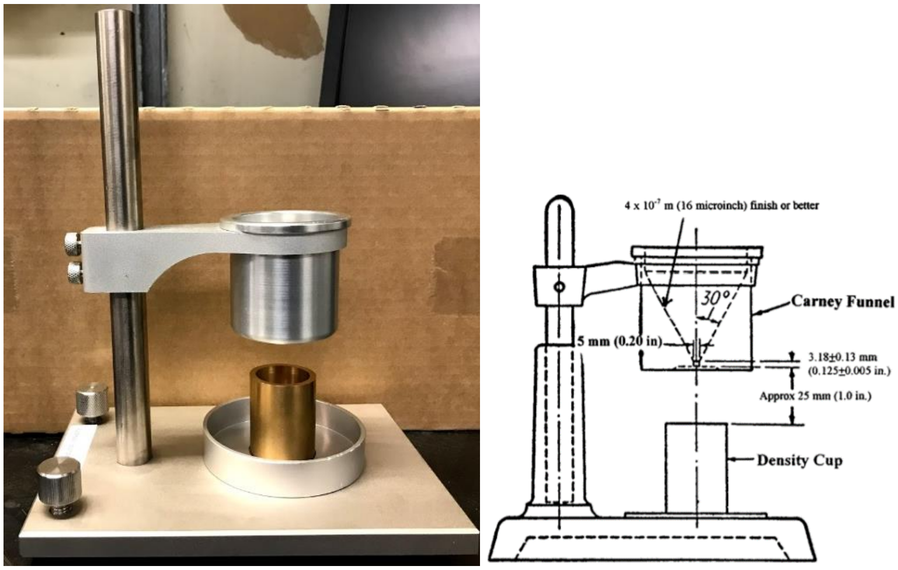

Figure 3.1 Hall flowmeter apparatus

Initially, 50 g of AerMet 100 powder were weighted and loaded into the flowmeter funnel. Then the time for the 50 g of powder to flow through the discharge orifice is recorded. The total time of discharge of the 50g of powder determines the powder flowability. To measure the powder apparent density, the density cup with a volume of 25 cm^3 is filled with loose powder. Then the powder in the density cup is weighted by using a laboratory scale and the mass of powder per unit volume is determined and reported as apparent density (AD_H). The measuring process is repeated three times to verify the repeatability of the measurement. The apparent density of the powder can be calculated by the below equation [3.1] and the results of apparent density and flowability are summarized in Table 3-1.

$$\mathrm{AD}_H = \frac{M}{V} = \frac{M}{25\ cm^3}$$

Where,

M = Mass of powder in the density cup (grams)

V = Volume of density cup (25 cm^3± 0.01)

Table 3-1 AerMet 100 powder flowability and apparent density

Powder	**Flowability**	**Apparent density**
	(s/50g)	**(%)**
AerMet 100	17.5	50.0

3.2.2 Particle Size Distribution

The AerMet 100 Powder particle size distribution was analyzed by a HORIBA LA-920 Laser Scattering Particle Size Analyzer. The HORIBA LA-920 Laser Scattering Particle Size analyzer is illustrated in the Figure 3.2.

1 g of AerMet 100 powder is mixed and suspended in the isopropyl alcohol then loaded into the analyzer. The mixture of powder and the suspension liquid is then passing through a detection area where He-Ne laser are diffracted, and the scattering patterns are received by the detectors. The particle diameters are calculated according to the Mie theory [3.3] and the results are shown in Figure 3.3 and summarized in Table 3-2. The composition of AerMet 100 was provided by the supplier.

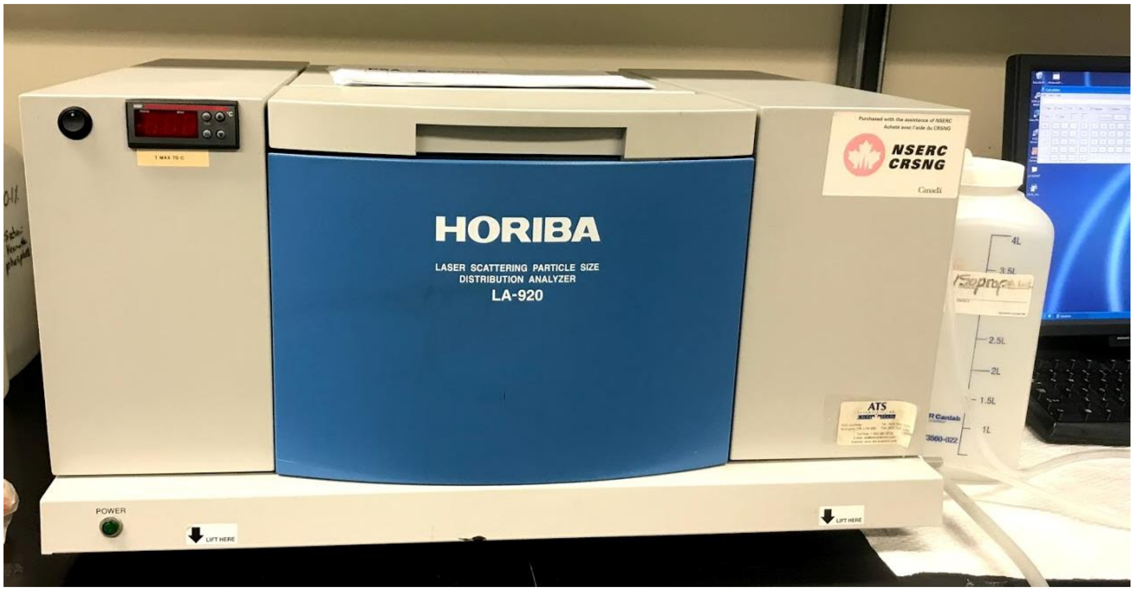

Figure 3.2 HORIBA LA-920 Laser Scattering Particle Size analyzer

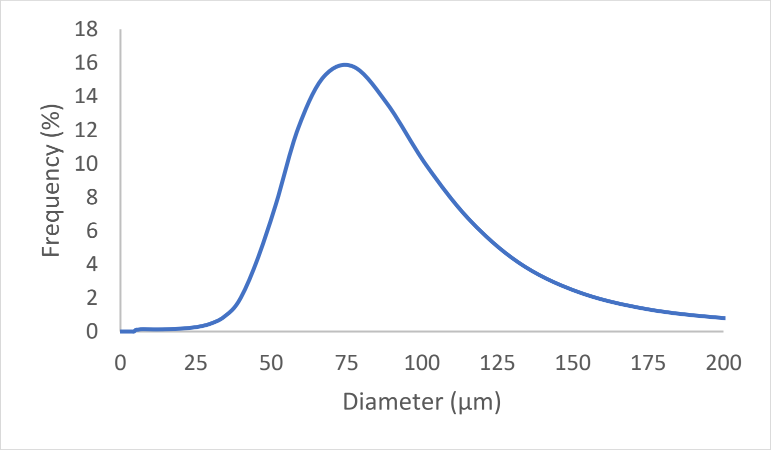

Figure 3.3 PSD of AerMet 100 powder

Table 3-2 Summary of AerMet 100

Composition (wt.%)						**Particle size (µm)**		
Fe	**C**	**Cr**	**Ni**	**Mo**	**Co**	**d10**	**d50**	**d90**
Bal	0.191	3.14	11.2	1.27	13.24	50	69	132

3.2.3 Powder Morphology and Alloy element distribution

AerMet 100 powder morphology was observed using a Hitachi SU3500 SEM. A small quantity of powder is blown gently to spread onto a carbon tape. Then the powder is placed into SEM chamber with vacuum environment to observe. AerMet 100 powder was mounted and sectioned for EDS analysis. And EDS is applied to study the alloy element distribution in the powder. According to the powder composition, C, Mo, Co, Ni, Cr are chosen to be the potential elements which may existed in the segregation. The Hitachi Su 3500 SEM equipped with EDS is illustrated in Figure 3.4.

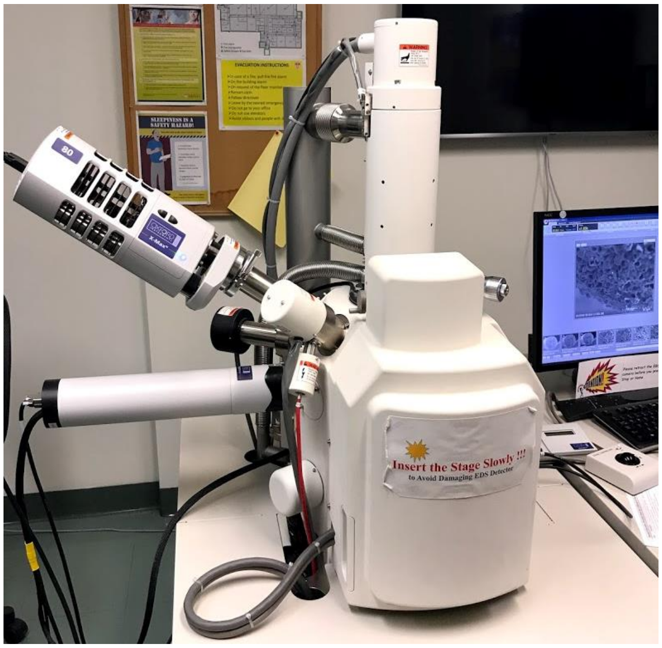

Figure 3.4 Hitachi SU3500 SEM equipped with EDS

3.3 Pulsed Laser Powder Bed Fusion (PLPBF) System

The AerMet 100 specimens in this study are fabricated by a custom built Pulsed Laser Powder Bed Fusion (PLPBF) system (Figure 3.5). The custom-built PLPBF system has a pulsed Nd:YAG laser source (λ=1064 nm) to fabricate cylindrical AerMet 100 specimens for microstructure studies. Figure 3.5 shows the configuration of the custom-built PLPBF system which includes an operation chamber with a control system. A camera is installed in the operation chamber to monitor the fabrication process and operation chamber is filled with argon for protection purpose.

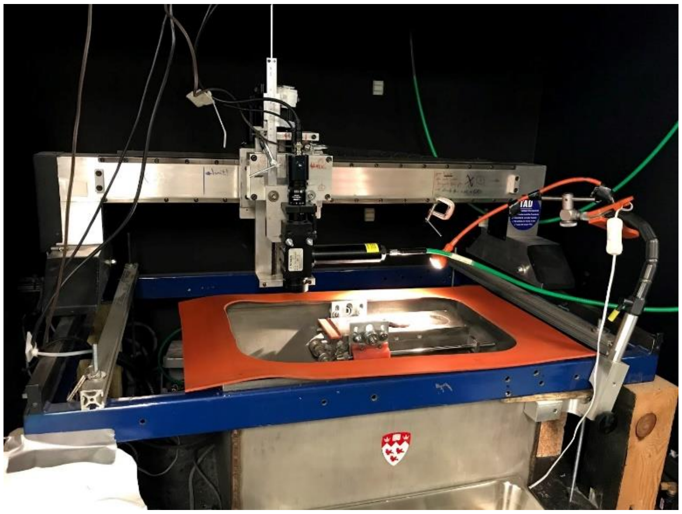

Figure 3.5 Custon-built PLPBF system

3.3.1 Laser Parameters

The custom-built PLPBF system was used in this study for AerMet 100 porosity optimization. This LPBF system is equipped with a 6000 W pulsed Nd:YAG laser source (λ = 1064 nm) with maximum exposure time of 10 ms, an automatic powder spreading system and an inert argon gas. The laser-related parameters, which are discussed in the previous chapter, include laser power, laser spot size, pulse duration and pulse frequency. A range of processing parameters, summarized in Table 3-3, was used to fabricate a series of AerMet 100 specimens. A rotational scanning strategy, illustrated in Figure 6, was adopted to fabricate the AerMet 100 specimens. The laser scans across the deposited powder initially at 90˚ direction in the xy-plane. The scanning direction was rotated by 90 ˚ in each subsequent layer until the fabrication process is completed.

Table 3-3 Laser parameters for AerMet 100

Parameters	Unit	
Peak Laser Power	W	1200
Exposure time	ms	1.7
Layer thickness	µm	75
Hatch Distance	µm	100
Frequency	Hz	20

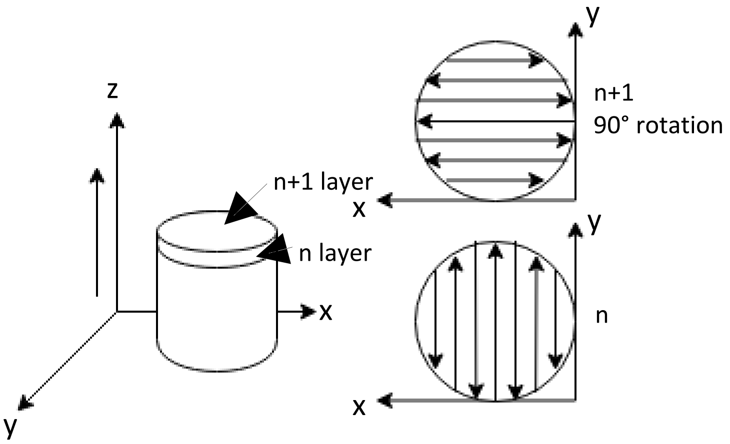

Figure 3.6 Scanning strategy

3.4 Heat Treatment

AM fabricated samples were subjected to two different heat treatments. The 3-stage heat treatment used for AerMet 100 includes 3 steps: (1) a solution heat treatment at a temperature of 885 °C in Ar environment for one hour followed by fan cooling. The purpose is to reach above Ac_3 temperature (829.4 °C) to form a solid solution. This is followed by a moderate cooling (fan cooling) to maintain this structure. (2) a cryogenic treatment at -73 °C for one hour followed by warming to room temperature in air to transform the retained austenite into martensite and (3) an aging treatment at 482 °C in an argon (Ar) environment for five hours followed by air cooling. It is reported that M_2C would be formed under this aging temperature to enhance both strength and fracture toughness [3.4].

The stress-relief heat treatment is to reduce the internal stress due to the uneven rapid cooling and existed defects during AM fabrication. During stress-relief heat treatment, decomposition of martensite may occur. However, it is possible to optimize the time and temperature for stress-relief heat treatment without jeopardizing the hardness[3.5]. The stress-relief treatment was carried out at 427 °C in an Ar environment for one hour followed by air cooling. A slow cooling speed is important to avoid residue stress build up caused by temperature differences in the material.

3.5 Sample Preparation

3.5.1 Mounting, Grinding and Polishing

To investigate the microstructure of AM fabricated samples, all samples were sectioned by using a diamond saw then the sectioned specimens were mounted and grinded by sequential grinding steps up to 1200 grit using silicon carbide abrasive papers. Afterwards, the grinded samples were subsequently polished by using diamond polishing pad with 9 µm, 3 µm, 1 µm and 0.5 µm diamond suspension.

3.5.2 Etching

To reveal the microstructure, 5% Nital was used as etchant. It is a solution of 5 ml HNO_3 + 95 ml alcohol and the samples were submerged in the solution for 1 to 2 minutes to reveal the microstructure. The etched Aermet 100 specimens were then washed by deionized water and dried by a blow-dryer.

3.6 Microscopic Examination

The sample quality and density condition were observed by a Nikon EPIPHOT 200 Light Optical Microscope (LOM) with Clemex Vision System (Figure 3.7) and analysed by the assistance of 2D image analysis tool ImageJ under low magnification. For high magnification observation, Hitachi SU 3500 scanning electron microscope (SEM) was used as illustrated in Figure 3.4. Characterized microstructural features observed by SEM included: cell size, grain size and dendrite arm spacing. Segregation during LPBF process was analysed by EDS.

Figure 3.7 Nikon EPIPHOT 200 Light Optical Microscope

3.7 X-Ray Diffraction Analysis

X-Ray Diffraction (XRD) analysis was applied in this study to identified phases in the powder, as-built sample and samples with corresponding heat treatments. Bruker D8 Discover XRD model (Figure 3.8) with Cu Kα radiation was employed and was operated at a voltage of 40kV, a current of 40mA, a step size of 0.005 and a total step time of 1200s.

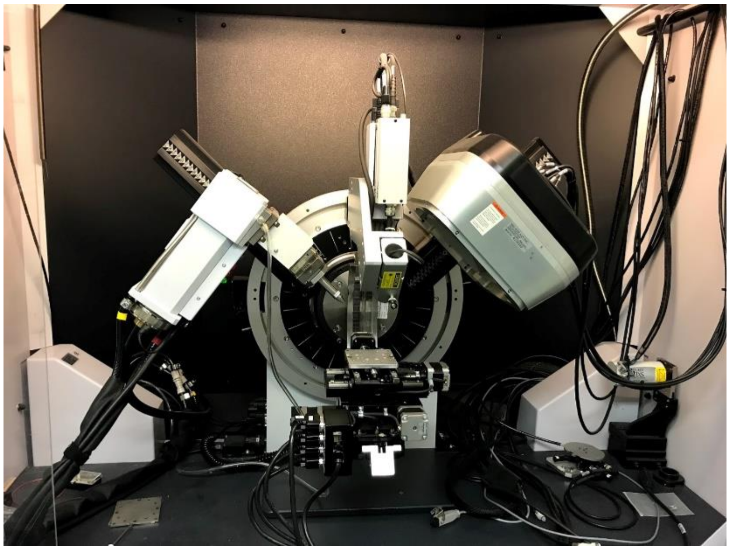

Figure 3.8 Bruker D8 Discover XRD model

3.8 Mechanical Properties Characterization

To compare the hardness of conventional wrought heat-treated sample and AM fabricated samples, Vickers hardness test was applied to as-built samples, samples with corresponding heat treatments and wrought heat-treated samples. According to ASTM E92-82 [3.6], the microhardness of all samples (conventional wrought heat-treated sample, AM fabricated as-built samples and AM fabricated samples with corresponding heat treatments) was measured by Clark Microhardness (CM-100AT) indenter, as shown in Figure 3.9, with a Vickers hardness scale of 500 gf and a 15 seconds indentation period. Multiple locations were chosen throughout tested samples and compared the same region in different condition samples.

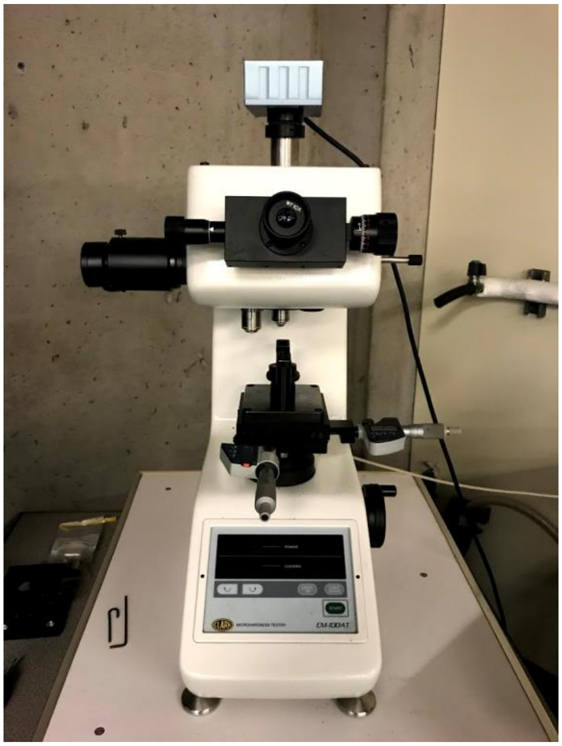

Figure 3.9 CM-100AT

3.9 Reference

3.1 ASTM B212-13, Standard Test Method for Apparent Density of Free-Flowing Metal Powders Using the Hall Flowmeter Funnel. 2013, ASTM International: West Conshohocken, PA.

3.2 ASTM B213-13, Standard Test Methods for Flow Rate of Metal Powders Using the Hall Flowmeter Funnel. 2013, ASTM International: West Conshohocken, PA.

3.3 Horvath, H., Gustav Mie and the scattering and absorption of light by particles: Historic developments and basics. Journal of Quantitative Spectroscopy and Radiative Transfer, 2009. **110**(11): p. 787-799.

3.4 Ayer, R. and P. Machmeier, On the characteristics of M2C carbides in the peak hardening regime of AerMet 100 steel. Vol. 29. 1998. 903-905.

3.5 Thelning, K.-E., 5 - Heat treatment—general, in Steel and its Heat Treatment (Second Edition). 1984, Butterworth-Heinemann. p. 207-318.

3.6 ASTM E92-82(2003), Standard Test Method for Vickers Hardness of Metallic Materials. 2003, ASTM International: West Conshohocken, PA.

Chapter 4: Pulsed Laser Powder Bed Fusion of AerMet 100

M. Chen, Y. Ding, X.Wang, M. Brochu

4.1 Preface

This chapter addresses the results of this work. An initial study was carried out to examine the feasibility of additive manufacturing AerMet 100 through evaluating the microstructural morphology and mechanical properties of specimens fabricated using a custom-built pulsed laser powder bed fusion (PLPBF) system. In addition to microstructural examinations, the elemental segregation of the AerMet 100 specimens in LPBF process was explored.

4.2 Abstract

Ultra-high strength steel AerMet 100 sample was fabricated by pulsed laser powder bed fusion (PLPBF) additive manufacturing process. Different heat treatments were applied to the as-deposited samples. The microstructure of build-up, heat affected zone (HAZ) and substrate with respect to as-deposited, stress-relieved and heat-treated samples were characterized using scanning electron microscopy (SEM), Energy-dispersive X-ray spectroscopy (EDS), and X-ray diffraction (XRD). The c/a ratio of martensite was calculated and compared under the different conditions. The XRD results indicated that the predominant phases in the build-up area of as-deposited condition are martensite and retained austenite. The Vickers hardness results showed a similar or superior hardness of all PLPBF produced samples when compared to the wrought AerMet 100 (606HV)[1]. Due to the thermal effect during AM process, the hardness decreased around the HAZ/build-up interface. Post PLPBF heat treatments greatly increased the hardness of the as-deposited samples. In comparison with as-deposited AerMet 100 sample, the existence Cr-rich $M_{23}C_6$ carbides in the stress-relieved sample strengthened the martensite matrix and thus resulted in an increased hardness; the elimination of retained austenite and homogenized martensitic structure in the heat-treated sample improved the hardness.

4.3 Introduction

AerMet® 100 alloy is a commercial ultra-high strength steel supplied by Carpenter Technology Corporation [4.1,4.2] for aerospace structural applications requiring a combination of high strength, high fracture toughness and good resistance to stress corrosion cracking [4.3]. Its nominal composition is 0.23% C, 3.1% Cr, 11.1% Ni, 1.2% Mo, 13.4% Co and balance Fe [4.4], and upon appropriate heat treatment yields the following mechanical properties: ultimate tensile strength (UTS): 1965 MPa, yield strength (YS): 1724 MPa, and Fracture toughness (K_{IC}): 126 MPa$\sqrt{m}$ [4.1]. The strength and fracture toughness properties of the cast AerMet 100 were found to be equal or superior of other existing high strength steels such as 300M, AISI 4340, Marage 250 and AF 1410 [4.4, 4.5].

The weldability of AerMet 100 is high compared to other types of high strength steel due to the fact that it has a relative high content of nickel, chromium and cobalt forming relatively soft and ductile martensite[4.6]. Highlights from the few available welding studies on AerMet 100 in the open literature include the following concepts. C. Westrich [4.7] demonstrated that both electron beam and laser beam welding produced high quality welds with no cracking or porosity in weld cross-sections. Work done by D. Englehart *et al.* [4.6] through electron beam (EB) welding process also indicates that for directly aged bead on the plate, the overaged region of the heat affected zone (HAZ) is the key area dictating strength while impact toughness is controlled by fusion zone. And post-welding heat treatment (PWHT) conditions is another alternative to provide optimized combination of strength and toughness. As reported by R. Ayer and P. Machmeier[4.8], relatively fine and undissolved carbides, (CrTiFeMo)C or MC and $(CrFeMo)_{23}C_6$ or $M_{23}C_6$, are dispersed in the martensitic matrix in the as-quenched condition. When tempering at 427 °C is imposed, a high density of cementite particles is formed due to the decomposition of martensite. The peak in strength is attained at a tempering temperature of 454 °C and this is because of the precipitation of coherent zones of fine carbides (M_2C)[4.9]. While the peak in toughness was attributed to the absence of cementite and the formation of reverted, stable austenite when tempering at 482 °C [4.8].

As shown above, some prior work has focused on the application of traditional welding of AerMet 100. These studies provided the theoretical support of applying additive manufacturing (AM) on AerMet 100. Since the martensite forming in this type (NI-Cr-Co steel) of alloy is relatively soft and ductile [4.6], this alloy should be resistant to the cold cracking phenomenon associated with the rapid cooling during AM process.

Pulsed Laser Powder Bed Fusion (PLPBF) is a new approach of selective laser melting (SLM) process with a pulsed-laser source [4.10] during which the powder particles are completely molten by the laser beam. Both high temperature gradients and high cooling rates (10^3-10^8 K/s) in the solid-liquid interface of moving molten pool enhance the formation of epitaxial growth dendritic solidification structure[4.11-4.13]; on the other hand, thermal cycling and heat accumulation effect after solidification cause the formation of complex as-deposited microstructure[4.12, 4.14, 4.15]. The utility of pulsed laser beam as heating source gives the principal advantages over continuous laser beam of changing weld pool geometries, heat flow stress field and refinement of the solidification structure [4.16]. Built objects are near full density with mechanical properties comparable to those matrix materials [4.17].

The objective of this study is to develop an understanding of the solidification metallurgy of AerMet 100 applicable to AM, the microstructure evolution under various heat treatment and compare the hardness in build-up, HAZ and substrate area under different heat treatment. The experimental validations included powder characterization, AM fabrication and PWHT, with the aim of fabricating crack-free parts.

4.4 Experimental procedures

The AerMet 100 powder from Carpenter Inc. (Reading, Pa), was used for powder characterization. The powders were characterized for (1) morphology with a Hitachi SU3500 scanning electron microscope (SEM), (2) alloy elements distribution by Energy-dispersive X-ray spectroscopy (EDS), (3) particle size distribution (PSD) with a LA-920 Horiba laser particle size analyzer, and (4) apparent density and flowability with Hall flowmeter following ASTM standards (B212-13 and B213-13)[4.18, 4.19].

Cylindrical samples of 5 mm in diameter were printed by a custom-built PLPBF unit. These samples were built with a layer thickness of 75 µm. PLPBF samples using AerMet 100 powder were carried out on wrought heat-treated AerMet 100 substrate. The schematic representation of PLPBF process print strategy is shown in Figure 4.1. The laser scans across the deposited powder started in the 90˚ direction in the xy-plane. The scanning direction was then rotated by 90 ˚ in each subsequent layer until the fabrication process was completed. The process was conducted under Ar environment.

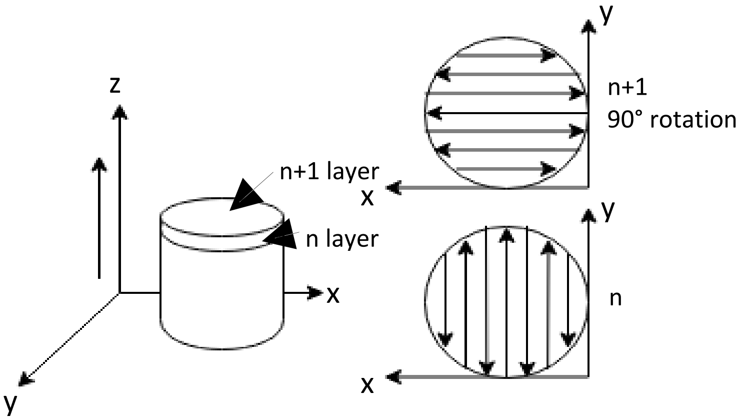

Figure 4.1 Schematic representation of PLPBF process

After deposition, the samples were subjected to two different heat treatments. The stress-relief treatment was carried out at 427 °C with Ar environment for one hour followed by air cooling. The 3-stage heat treatment of AerMet 100 includes 3 steps: (1) a solution heat treatment at a temperature of 885 °C in an Ar environment for one hour followed by fan cooling. (2) a cryogenic treatment at -73 °C for one hour followed by warming to room temperature (3) an aging treatment at 482 °C in an Ar environment for five hours followed by air cooling.

Upon printing, the samples were followed by sequential grinding steps up to 1200 grit using silicon carbide abrasive papers, and standard polishing steps up to 1 µm. The polished samples were etched in a solution of 5 ml HNO_3 + 95 ml alcohol for 1 to 2 minutes to reveal the microstructure. The microstructure evolution was characterized using a Hitachi SU3500 SEM equipped with electron dispersive spectrometer (EDS) and Hitachi SU8000 SEM for higher magnification to observe carbides. The SEM micrographs were all taken along the building direction for as-deposited, stress-relieved and heat-treated samples.

The phase present in the AerMet 100 powder, as-deposited, stress-relieved and heat-treated samples were identified by X-ray diffraction (XRD) method using Bruker D8 Discover model with Cu Kα radiation operated at a voltage of 40kV, a current of 40mA, a step size of 0.005 and a total step time of 1200s.

According to ASTM E92-82 [4.20], the microhardness of different condition samples (As-deposited, Stress-relieved, Heat-treated) was measured by means of a Clark Microhardness (CM-100AT) indenter with a Vickers hardness scale using 500 gf and a 15 seconds indentation period. Sixteen different locations in the same sample including build-up area, HAZ and substrate area were measured and compared with the same region in different condition samples.

4.5 Results and Discussion

4.5.1 Powder characterization

The powder size distribution (PSD) is shown in Figure 4.2. The morphology of the AerMet 100 powder is presented in Figure 4.3. The powder was mainly spherical with a few particles of irregular shape, some agglomerate and few with "satellite" particles. The powder characterization results are summarized in Table 4-1.The composition (wt.%) of the powder was provided by the supplier. D_{10}, D_{50} and D_{90} are with respect to 50 µm, 69 µm and 132 µm. The powder flowability was 17.5s/50g and it was governed by the morphology and size distribution. The apparent density is 3.95 g/cm^3, and it was 50.1% of full density of AerMet 100 (7.889 g/cm^3)[1]. The better the packing density, the better consolidation during processing.

The microstructure of the as-received powder is presented in Figure 4.5. A cellular-like structure was observed. XRD results (Figure 4.4) show that the predominant phase was martensite, with only trace amount of retained austenite, which indicates the cooling rate during powder fabrication was sufficiently fast (>3.3°C/s)[4.1]. EDS mapping shown in Figure 4.6 depicting the enrichment of Cr and Mo in the grain boundary area. There was no obvious enrichment of Co and Ni in the selected area.

Table 4-1 Summary of AerMet 100 Powder characterization

Composition (wt.%)						**Particle size (µm)**			**Flowability**	**Apparent density**
Fe	**C**	**Cr**	**Ni**	**Mo**	**Co**	**d10**	**d50**	**d90**	**(s/50g)**	**(%)**
Bal	0.191	3.14	11.2	1.27	13.24	50	69	132	17.5	50.1%

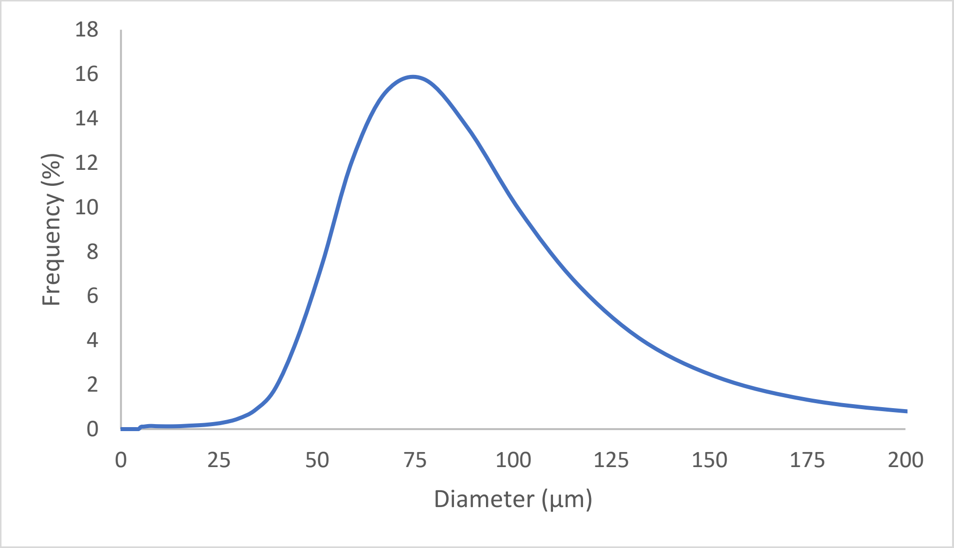

Figure 4.2 PSD of AerMet 100 powder

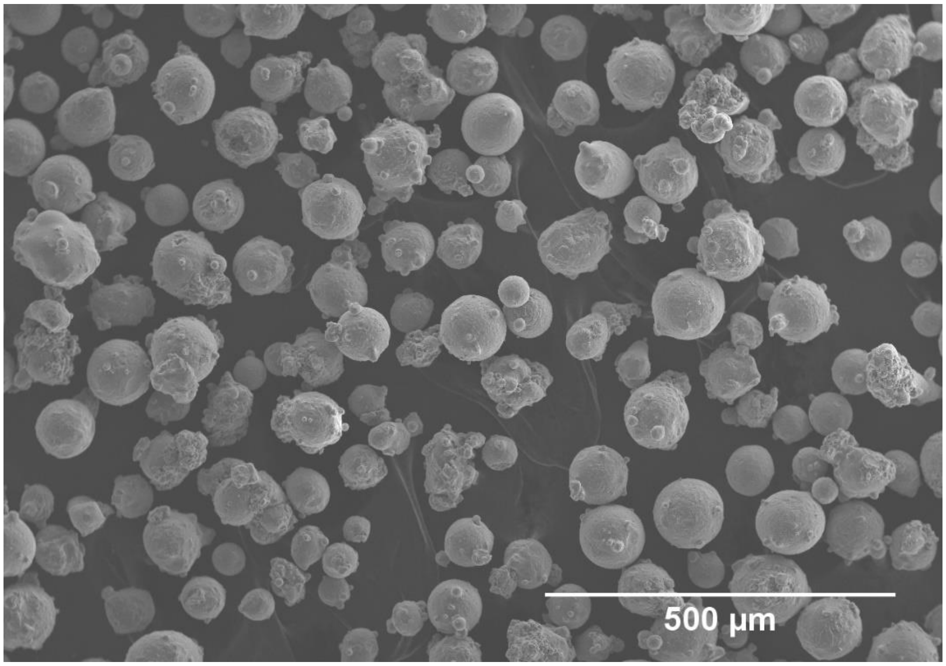

Figure 4.3 SEM Secondary Electron(SE) image of AerMet 100 powder at 100X

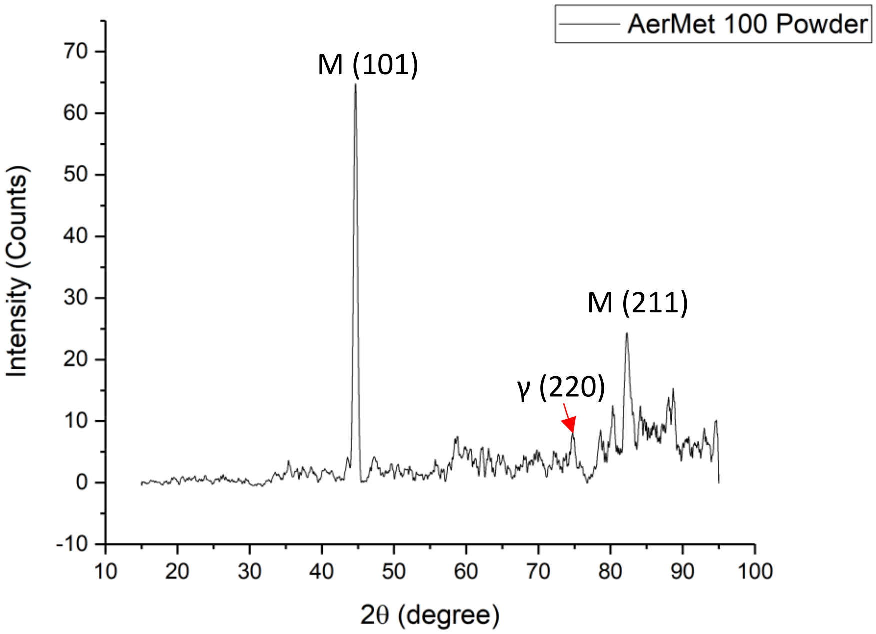

Figure 4.4 AerMet 100 powder XRD result, M: martensite

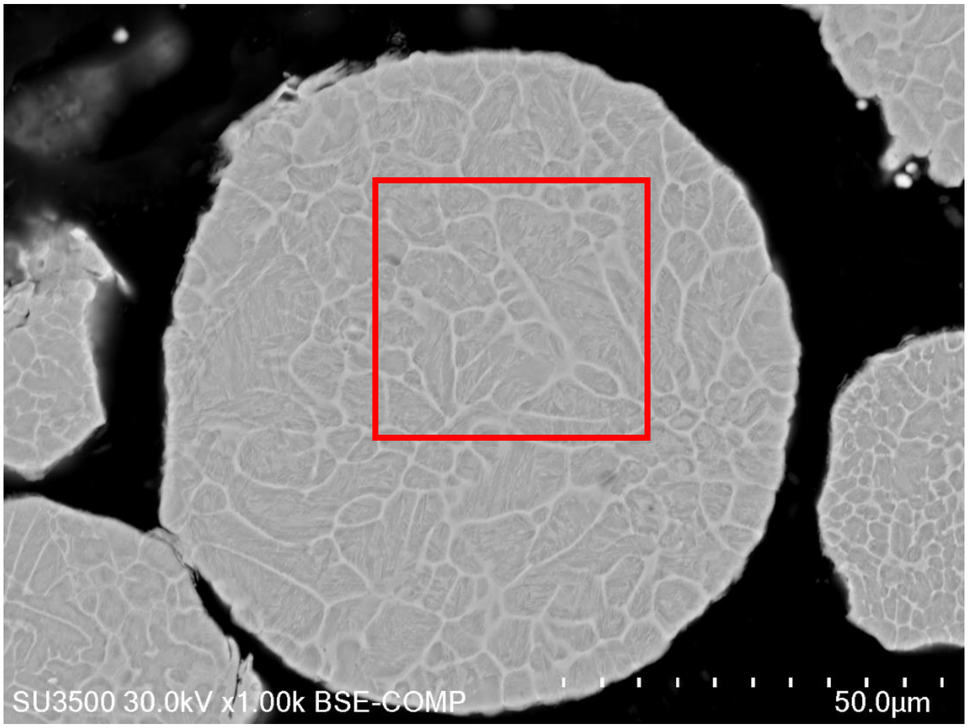

Figure 4.5 Microstructure of AerMet 100 powder

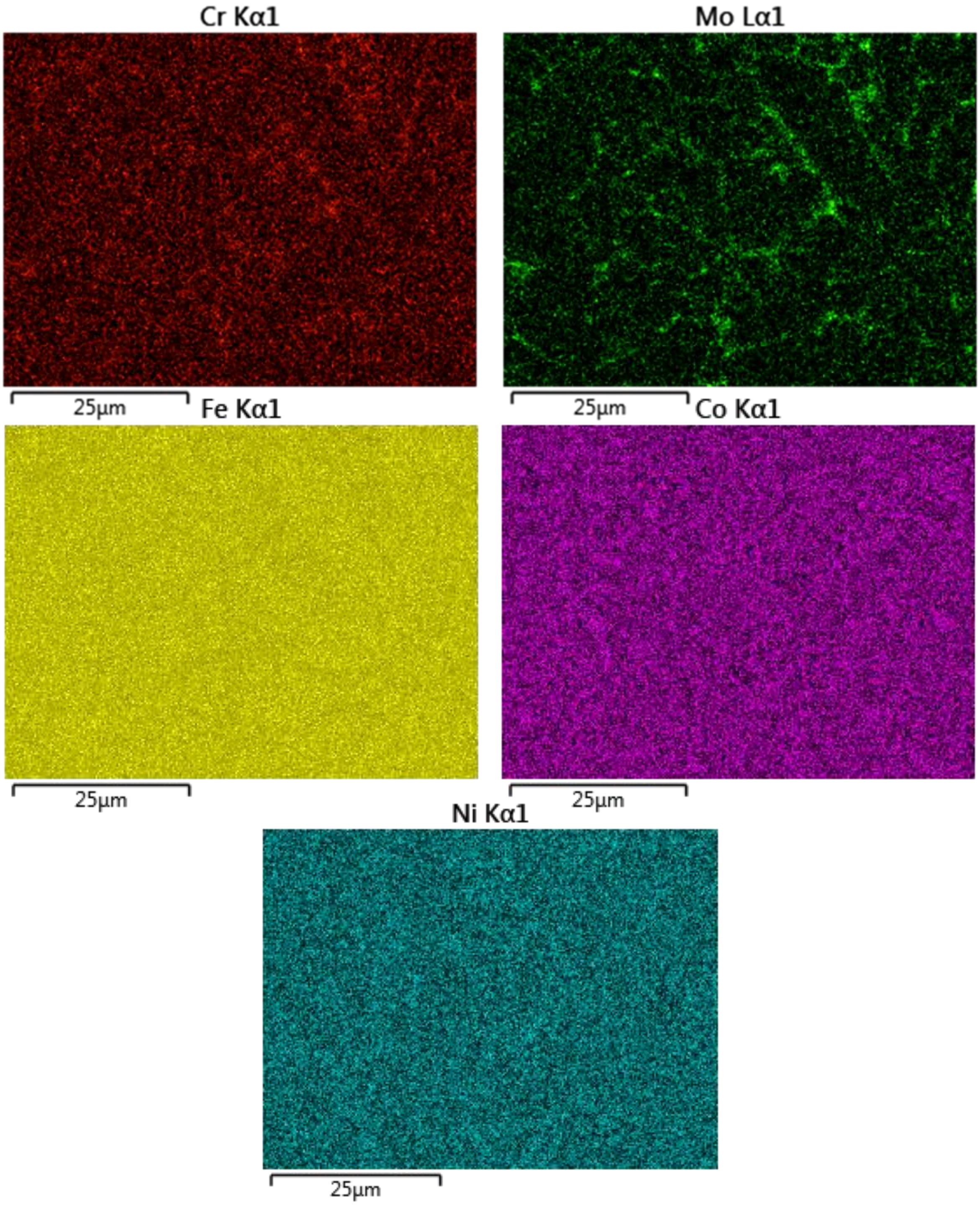

Figure 4.6 EDS mapping of selected area (red) in Figure 4.5

4.5.2 Microstructure characterization

4.5.2.1 As-deposited sample

Scanning electron microscopy (SEM) was applied to reveal the microstructure of as-deposited sample and the results are shown in Figure 4.7. The fine microstructure of the build-up area was the result of rapid cooling. Figure 4.7A depicts an over view of a section covering the build-up to substrate. Figure 4.7B shows a detailed microstructure of build-up area, which was free of cracks. It exhibits a martensite matrix (dark area in Figure 4.7B) and a long-plate structure (bright area in Figure 4.7B) due to martensitic transformation and segregation of the alloy elements. The average dendrite arm spacing is 1.16±0.33 µm in the build-up. This microstructure presents continuous secondary phases segregated in the inter-dendritic regions, most of which are Cr and Mo elements (Table 4-2). The similar microstructure is reported in the literature with laser cladded AerMet 100 [4.21]. Apart from martensite, retained austenite peaks were observed in the XRD results showed in Figure 4.10. This is due to the increased alloying element in the segregation region [4.22], martensite transformation start temperature (M_s) and finish temperature (M_f) reduction occurred, causing the retained austenite left at room temperature [4.23]. By analysis through ImageJ software, about 15% of retained austenite existed in the build-up area (bright area). Since this was a multi-layer-pass deposition, the precipitation of small carbides happens due to the heat accumulation, which gives carbon extra diffusion time. According to the previously reported data [4.8, 4.12], these carbides may be of the MC and $M_{23}C_6$ type. These carbides can be observed in the SEM images (Figure 4.7E) but not in XRD results due to the insufficient quantity (<5%) to be detected. Figure 4.7C presents a tempered martensitic structure in HAZ because of multiple thermal cycles experienced during the AM process, the grains were coarsened due to the thermal effect. Figure 4.7D presents lath martensite structure in the conventional wrought substrate which has a completely different morphology as martensite in the build-up.

Table 4-2 EDS results of alloy elements in dendrite arm and inter-dendritic region of as-deposited build-up area corresponding with Figure 4.7B

Position	Mark	Co (wt%)	Ni (wt%)	Cr (wt%)	Mo (wt%)
Bright region	Spectrum 1	12.7	10.2	3.3	1.4
Dark region	Spectrum 2	12.6	10	2.7	1

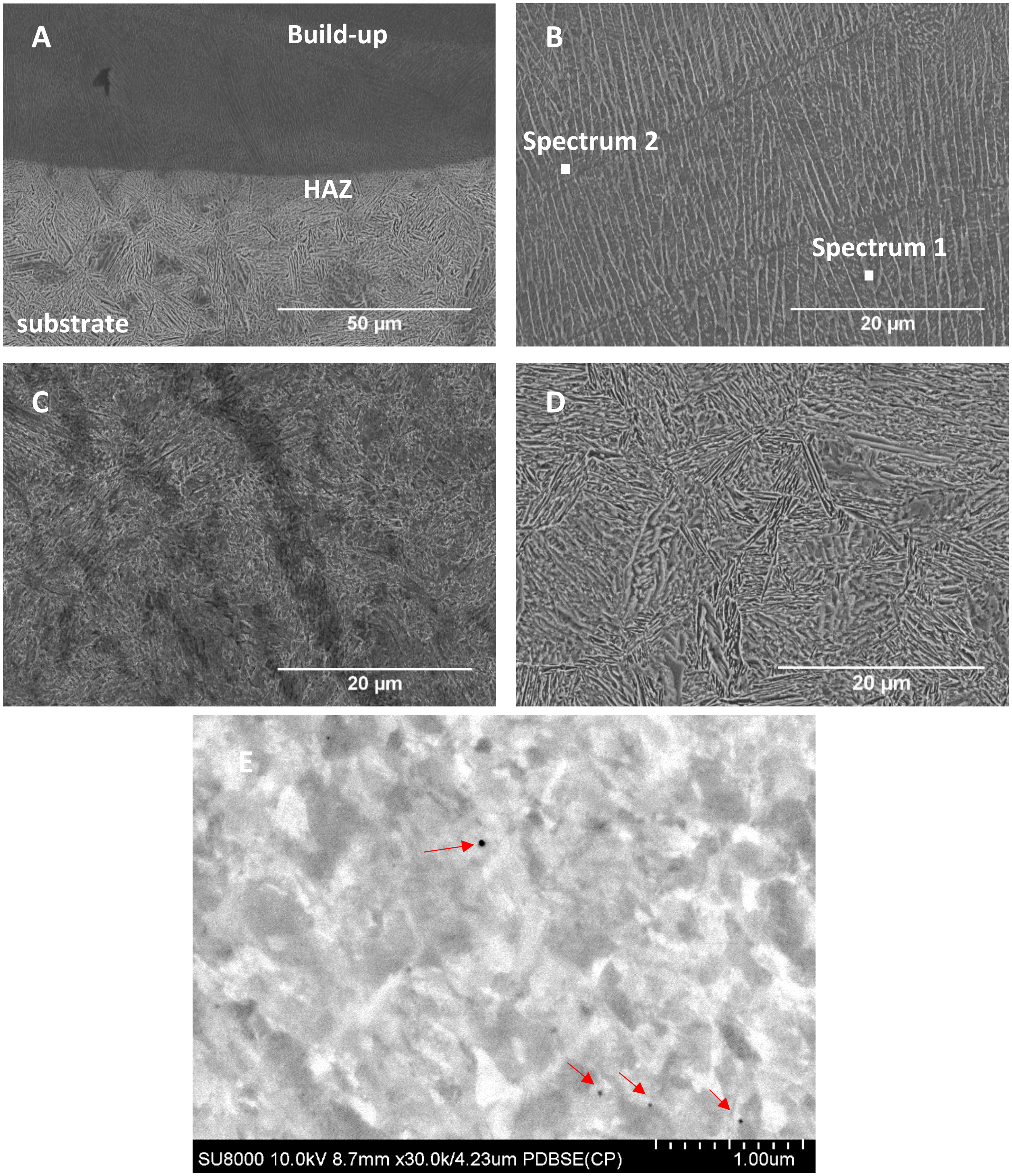

Figure 4.7 SEM image of as-deposited sample, A: Over view of build-up, HAZ and substrate; B: build-up area; C: HAZ; D: Substrate; E: Carbides (black dots) observed in the build-up

4.5.2.2 Stress-relieved sample

In the stress-relieved condition, the morphology of microstructures with respect to build-up, HAZ and substrate (Figure 4.8A) did not significantly change since the temperature of stress relief is at 427 °C, which is below the Ac_1 temperature (573.9 °C)[4.1]. Same amount of martensite (dark region) and retained austenite (bright region) existed in the build-up area according to the XRD results. Besides, under the effect of a temperature of 427 °C and a dwell time of 1h, an increased amount (about four times more) of the Cr-rich $M_{23}C_6$ carbides were both observed and identified within the structures (Figure 4.8E, Figure 4.10) as the amount of carbides increased as the temperature increased [4.24]. There is no cementite observed in the stress relieved sample. This is inconsistent with the study of R. Ayer and P. Machmeier, as they tempered the alloy for five hours comparing with one-hour stress relief in this study. Moreover, in the bright region (Figure 4.8B) of EDS, some segregation of Cr and Mo elements was observed (Table 4-3) and revealed where carbides were located. Same as the as-deposited sample, martensite transformation start temperature (M_s) and finish temperature (M_f) reduction occurred in the bright region, causing the retained austenite left at room temperature [4.23]. The average size of dendrite arm spacing (bright area) is 1.14±0.44 µm in the build-up area. Figure 4.8C presents a tempered martensitic structure with coarsened grains due to the thermal accumulation effect in HAZ and Figure 4.8D presents lath martensite structure in the substrate.

Table 4-3 EDS results of alloy elements in dendrite arm and inter-dendritic region of as-deposited build-up area corresponding with Figure 4.8B

Position	Mark	Co (wt%)	Ni (wt%)	Cr (wt%)	Mo (wt%)
Bright region	Spectrum 1	12.4	10	3.2	1.3
Dark region	Spectrum 2	12.3	10.1	2.8	1

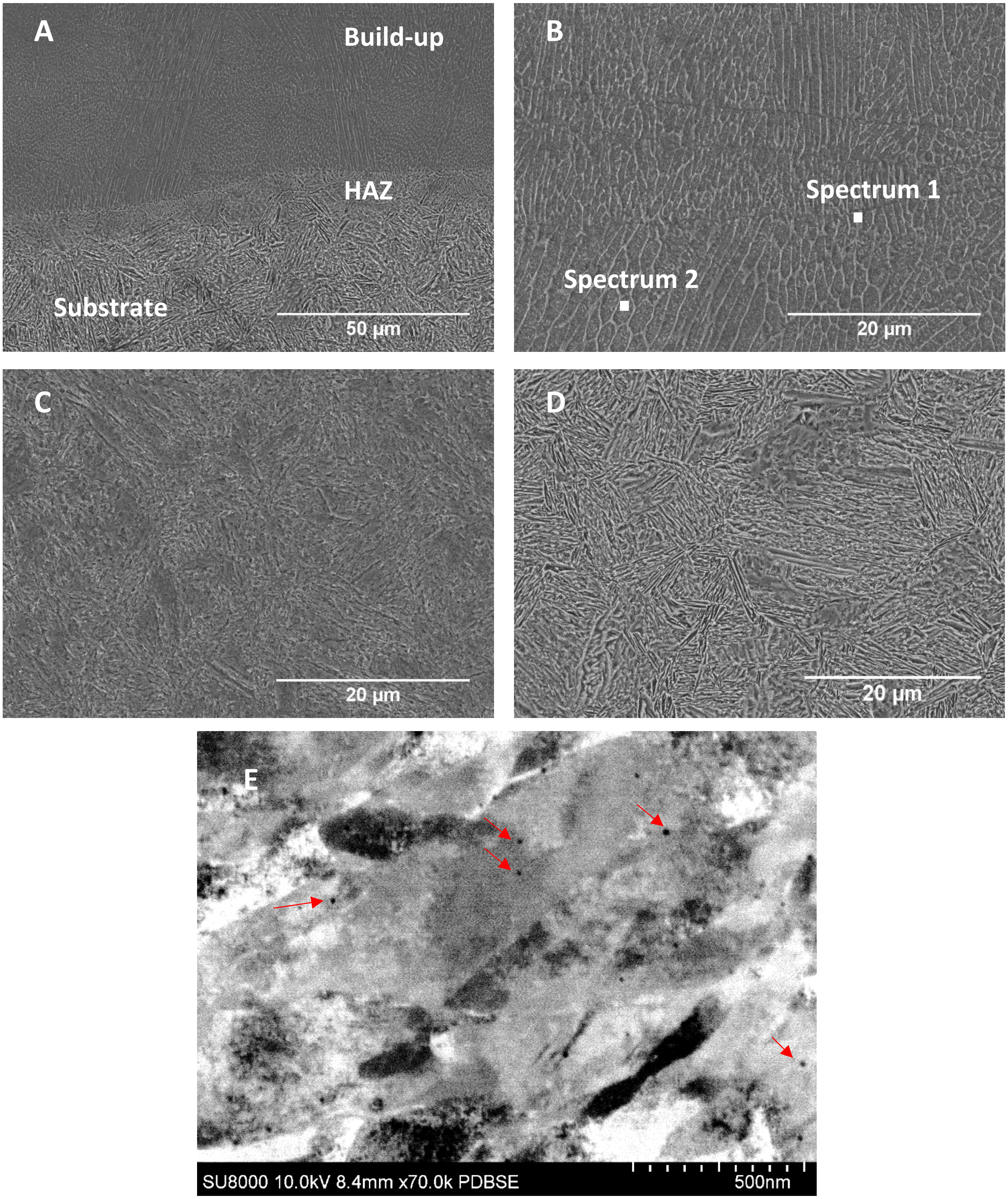

Figure 4.8 SEM image of stress-relieved sample, A: Over view of build-up, HAZ and substrate; B: build-up area; C: HAZ; D: Substrate; E: Carbides (Black dots) observed in the build-up

4.5.2.3 Heat-treated sample

In the heat-treated condition, there was no apparent boundary between build-up area, HAZ and substrate. The microstructure in Figure 4.9A *to* Figure 4.9D was very similar to the one presented in Figure 4.8C and Figure 4.7C, showing the microstructure of lath martensite in the prior austenite grain. The first step was heat treated for an hour at 885 °C which is higher than the Ac_3 temperature of AerMet 100 (829.4 °C) [4.1], therefore creating a homogenized microstructure. According to previous research [4.25, 4.26], the morphology of lath martensite varies with the amount of carbon dissolved in the austenite but the formation of lath martensite causes by slipping [4.27]. The martensite was transformed from austenite during the fan cooling after the first step of the heat treatment. Afterwards, in the second step, a cryogenic treatment was applied to transform the retained austenite in to martensite. In the third step, the purpose of ageing process is to reach optimal combination of strength and toughness. As the high temperature and long dwell time, the microstructure of heat-treated sample shows the existing martensite has been tempered. It is reported that both fine M_2C carbide and reverted austenite existed in the heat-treated sample [4.8, 4.9, 4.28]. However, XRD results (Figure 4.10) show that the predominant phase after the 3-step heat-treatment was martensite, and no peaks of retained austenite and carbides were observed.

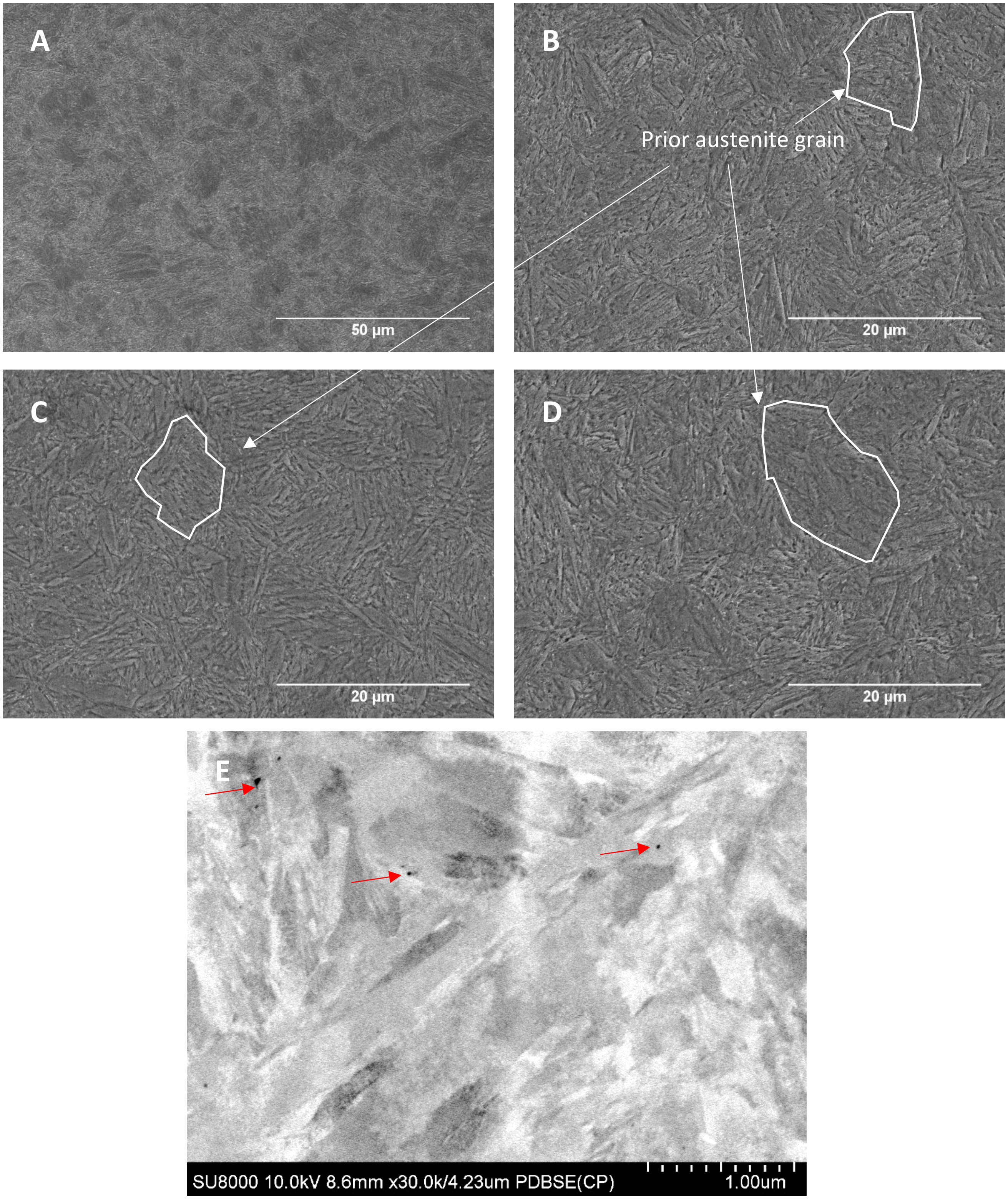

Figure 4.9 SEM image of Heat-treated sample, A: Over view of build-up, HAZ and substrate; B: build-up area; C: HAZ; D: Substrate; E: Carbides (black dots) observed in the build-up

4.5.3 XRD Analysis

As presented in Figure 4.10, martensite peaks were observed in all four tested samples. Retained austenite peaks were observed in as-deposited and stress-relieved samples and $M_{23}C_6$ carbides were also detected in the stress-relieved sample. The c/a ratio of the four studied conditions and a comparison from the literature are listed in

Table 4-4. The results showed that the as-deposited sample had the highest c/a ratio, indicating an high tetragonality martensite microstructure. As the stress relief and heat treatment applied, the c/a ratio decreased with an increasing tempering temperature. This means that the microstructure had been tempered in stress-relieved and heat-treated samples and the martensite in these samples had less tetragonality. One reason to explain the similarity of the calculated c/a ratio of the powder and heat-treated samples with the data of Ran *et al.* [4.15] is their cooling rate close to atomization. Therefore, the carbon has more time to diffuse, resulting in a lower c/a ratio. According to O. Sherby *et al.* [4.29], only primary martensite will form during the quenching of Fe-C steel below 0.6 wt% C (designated as H point) and it is created through the two sequential steps FCC (face-centered cubic) to HCP (hexagonal close-packed) followed by HCP to BCC (body-centered cubic). Primary martensite has a lath structure and described as BCC iron containing a C-rich phase that precipitates during quenching. Above the H point, primary martensite keeps forming with the creation of a C-rich BCT (body-centered tetragonal) phase. This is followed by the start of secondary martensite and creates the traditional BCT phase adjoining retained austenite at M_s temperature. However, the value of the H point can be influenced by changes in alloy content or by processing conditions. Winchell and Cohen [4.30] have shown that large Ni additions will decrease the H point to about 0.2 wt% C. Moreover, very high cooling rates, for example in excess of 30,000 °C/s, enabled the formation of BCT martensite in the low carbon range (below 0.6 wt% C) [4.29]. The results of Cadeville *et al.* [4.31] also showed X-ray evidence for a BCT structure at carbon contents with a H point at 0.2 wt% C. In this research, retained austenite is observed in the as-deposited and stress-relieved samples and the relative higher c/a ratio indicates a higher carbon content and a higher cooling rate. Therefore, both primary and secondary martensite are existed in the as-deposited and stress-relieved samples as retained austenite was detected. In heat-treated sample, the predominant phase was primary martensite with only possible trace amount of secondary martensite since the c/a ratio close to 1, which represent BCC crystalline structure.

Table 4-4 Calculated c/a ratio of all samples

Sample	Powder	As-dep	SR	Hted	Ran et al[15]
c/a ratio	1.0018	1.0046	1.0034	1.0017	1.0014

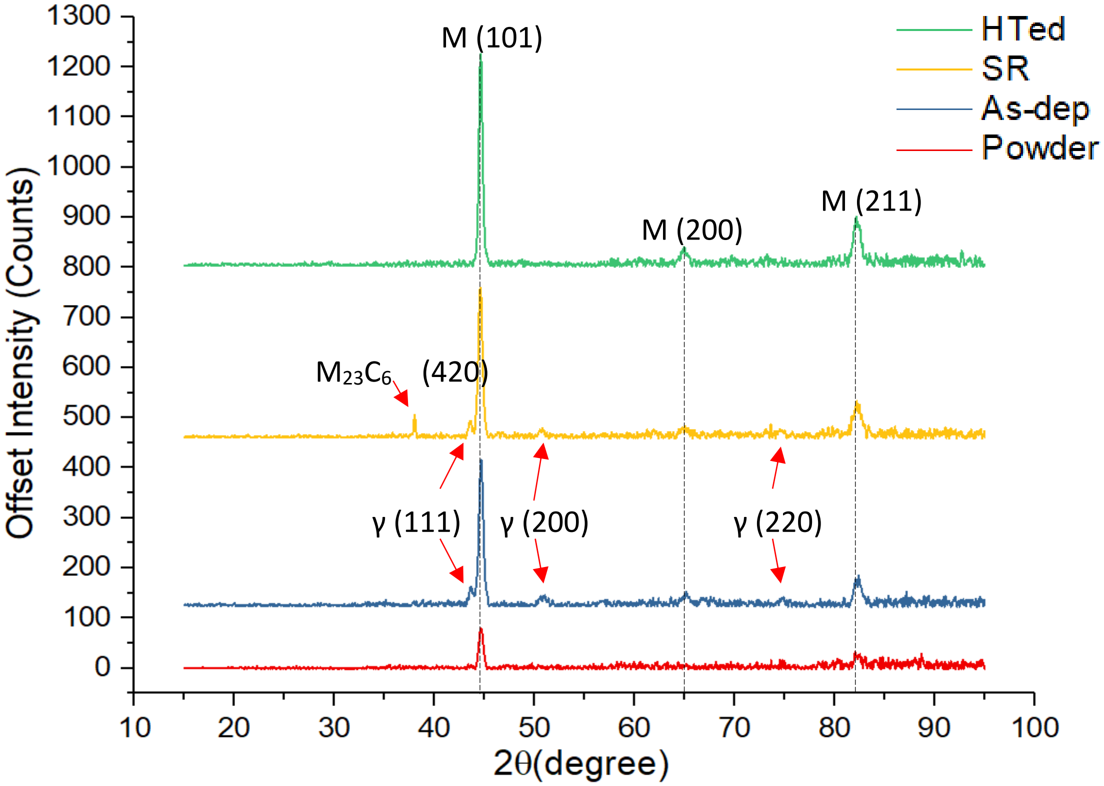

Figure 4.10 XRD results corresponding to four samples, As-dep: As-deposited, SR: stress-relieved, HTed: heat-treated

4.5.4 Hardness testing

The hardness distribution of AerMet 100 with different conditions is presented in Figure 4.11. The reference material was wrought heat-treated AerMet 100 with a hardness of 621±2 HV. In the as-deposited sample, the average hardness is 560±31 HV and the peak hardness with 600 HV occurred in the build-up region where far from HAZ/build-up interface. The hardness values fell from the peak value in the build-up region until it reached HAZ/build-up interface with the lowest hardness value of 500HV. The hardness of HAZ fell from substrate/HAZ interface to HAZ/build-up interface from 578HV to 500HV. The reason of HAZ and build-up hardness lower than the substrate is because of the retained austenite. The low hardness value in the region of the HAZ adjacent to the parent material was probably due to grain coarsening caused by overaging. In the stress-relieved sample, the hardness of HAZ and build-up has significantly increased. The existence of $M_{23}C_6$ carbide as detected in the XRD results is clearly an indication of the contribution in strengthening the martensitic matrix [4.32].The overall hardness of stress-relieved sample was 627±14 Hv which is coherent with the reference value. This means that stress relief treatment helped AM fabricated AerMet 100 reaching a desired hardness. Lastly, the average hardness for heat-treated sample was 614±20 Hv. It was similar to the reference material processed under the same heat treatment. In addition, the hardness of martensite is highly influenced by carbon. It can explain why the overall hardness of build-up region was slightly lower than the substrate among all samples as the powder used for PLPBF process contained relatively lower amount of carbon than the substrate material.

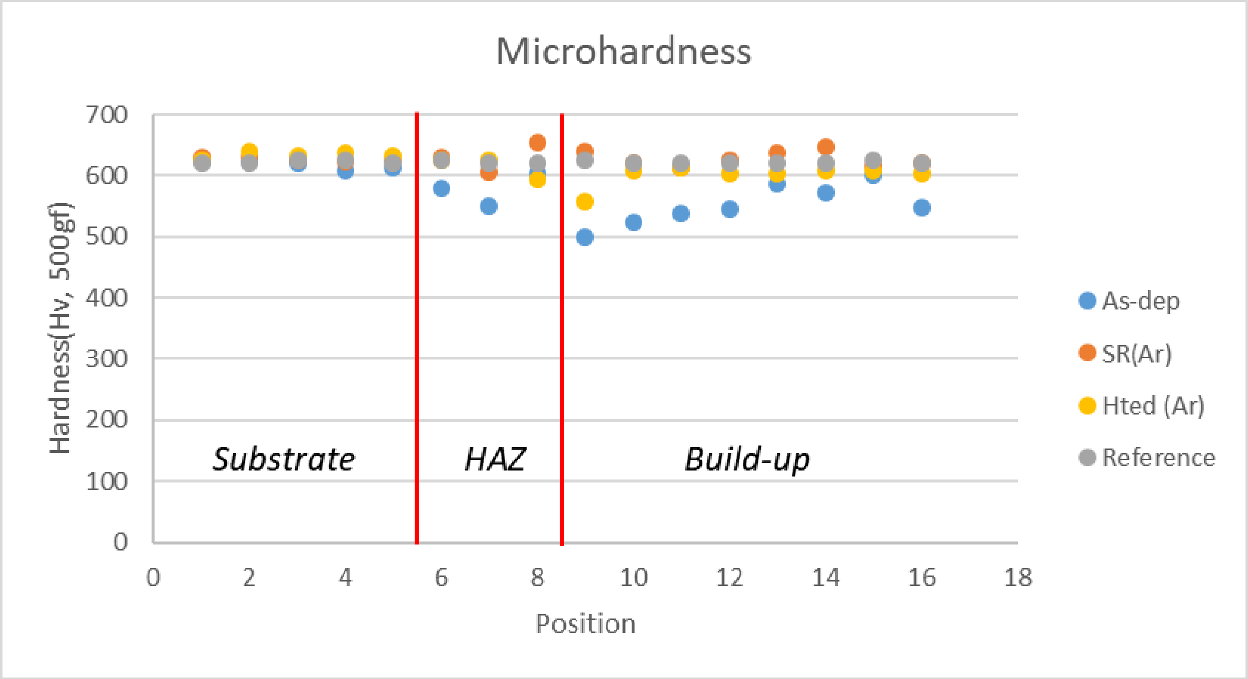

Figure 4.11 Microhardness distribution of as-deposited, stress-relieved and heat-treated AerMet 100, Reference: wrought heat-treated sample

4.6 Summary

In this paper, the microstructure evolution and mechanical property of PLPBF fabricated as-deposited, stress-relieved and heat-treated AerMet 100 samples were investigated. In the as-deposited sample, a cellular dendritic-like structure was observed to grow along the heat gradient and building direction. The build-up area was predominately martensite with 15% retained austenite. Cr and Mo segregation was detected by EDS in the region where retained austenite existed. Carbides were observed under SEM. A coarsened tempered martensitic structure close HAZ/build-up interface was observed due to multiple thermal cycles heat accumulation during the AM process. In the stress-relieved sample, the microstructure did not change significantly when compared with the as-deposited condition. However, XRD results confirmed an increasing amount of $M_{23}C_6$ precipitation. In the heat-treated sample, the microstructure was homogenized to tempered martensite with a crystalline structure of BCC. Retained austenite was removed after heat treatment. The cooling rate has a significant impact on the tetragonality (c/a ratio) of the martensite structure. A higher cooling rate resulted in a higher tetragonality since the carbon atoms did not have enough to diffuse into the structure. Moreover, a comparison of hardness among as-deposited, stress-relieved and heat-treated samples revealed that the existence of $M_{23}C_6$ significantly increased the hardness of stress-relieved sample. Heat-treated samples also exhibited a competitive hardness due to the completed martensite transformation.

4.7 Acknowledgement

The authors would like to thank Dr. Yuan Tian for his great help with analysis consultation and appreciate Mr. Nicolas Brodusch and Mr. Frédéric Voisard for their great help of SU8000 SEM analysis.

4.7 Reference

4.1 *AerMet 100 Alloy Technical Datasheet*, C.T. Corporation, Editor. 2011.

4.2 Hemphill, R.M. and D.E. Wert, *High strength, high fracture toughness structural alloy*. 1992, Google Patents.

4.3 Novotny, P.M. and T.J. McCaffrey, *An Advanced Alloy for Landing Gear and Aircraft Structural Applications - Aerometr® 100 Alloy*. 1992, SAE International.

4.4 Schmidt, M.L., *AerMet® 100 Alloy for Landing Gear Applications-A Summary of Forging Studies*. 1992, SAE International.

4.5 Lippard, H.E., *et al.*, *Microsegregation behavior during solidification and homogenization of AerMet100 steel.* Metallurgical and Materials Transactions B, 1998. **29**(1): p. 205-210.

4.6 ENGLEHART, D.A., *et al.*, *Fusion Welding of AerMet 100 Alloy*. 1999, ; Sandia National Labs., Albuquerque, NM (US); Sandia National Labs., Livermore, CA (US). p. Medium: P; Size: 63 pages.

4.7 Westrich, C. and C.A. Lawrence Livermore National Lab, *Weldability of AerMet 100*. 1990, United States.

4.8 Ayer, R. and P. Machmeier, *Transmission electron microscopy examination of hardening and toughening phenomena in Aermet 100.* Metallurgical and Materials Transactions A, 1993. **24**(9): p. 1943-1955.

4.9 Ayer, R. and P. Machmeier, *On the characteristics of M2C carbides in the peak hardening regime of AerMet 100 steel*. Vol. 29. 1998. 903-905.

4.10 Chou, R., *et al.*, *Additive Manufacturing of Al-12Si Alloy Via Pulsed Selective Laser Melting.* JOM, 2015. **67**(3): p. 590-596.

4.11 Sun, S., M. Brandt, and M. Easton, *2 - Powder bed fusion processes: An overview*, in *Laser Additive Manufacturing*. 2017, Woodhead Publishing. p. 55-77.

4.12 Ran, X.-z., *et al.*, *Effects of post homogeneity heat treatment processes on microstructure evolution behavior and tensile mechanical properties of laser additive manufactured ultrahigh-strength AerMet100 steel.* Materials Science and Engineering: A, 2018. **723**: p. 8-21.

4.13 Jones, H., *Microstructure of rapidly solidified materials.* Materials Science and Engineering, 1984. **65**(1): p. 145-156.

4.14 Parimi, L.L., *et al.*, *Microstructural and texture development in direct laser fabricated IN718.* Materials Characterization, 2014. **89**: p. 102-111.

4.15 Ran, X., *et al.*, *Microstructure characterization and mechanical behavior of laser additive manufactured ultrahigh-strength AerMet100 steel.* Materials Science and Engineering: A, 2016. **663**: p. 69-77.

4.16 Tian, Y., J.A. Muñiz-Lerma, and M. Brochu, *Nickel-based superalloy microstructure obtained by pulsed laser powder bed fusion.* Materials Characterization, 2017. **131**: p. 306-315.

4.17 Kruth, J.P., *et al.*, *Selective laser melting of iron-based powder.* Journal of Materials Processing Technology, 2004. **149**(1): p. 616-622.

4.18 *ASTM B212-13, Standard Test Method for Apparent Density of Free-Flowing Metal Powders Using the Hall Flowmeter Funnel*. 2013, ASTM International: West Conshohocken, PA.

4.19 *ASTM B213-13, Standard Test Methods for Flow Rate of Metal Powders Using the Hall Flowmeter Funnel*. 2013, ASTM International: West Conshohocken, PA.

4.20 *ASTM E92-82(2003), Standard Test Method for Vickers Hardness of Metallic Materials*. 2003, ASTM International: West Conshohocken, PA.

4.21 Liu, J., *et al.*, *Microstructures and tensile properties of laser cladded AerMet100 steel coating on 300M steel.* Journal of Materials Science & Technology, 2018. **34**(4): p. 643-652.

4.22 Gualco, A., *et al.*, *Effect of post-weld heat treatment on wear resistance of martensitic steel hardfacing deposits*. Vol. 24. 2010. 258-265.

4.23 Lippold, J.C. and D.J. Kotecki, *Welding metallurgy and weldability of stainless steels*. 2005, Hoboken, NJ: John Wiley.

4.24 Lee, J.B., *et al.*, *Kinetics of carbide formation for quenching and tempering steels during high-frequency induction heat treatment.* Materials Chemistry and Physics, 2011. **129**(1): p. 365-370.

4.25 Bhadeshia, H.K.D.H. and S.R. Honeycombe, *5 - Formation of Martensite*, in *Steels (Third Edition)*. 2006, Butterworth-Heinemann: Oxford. p. 95-128.

4.26 Verhoeven, J.D., *Steel metallurgy for the non-metallurgist.* 2007.

4.27 Krauss, G. and A. Marder, *The morphology of martensite in iron alloys.* Metallurgical Transactions, 1971. **2**(9): p. 2343.

4.28 Shi, X., *et al.*, *Study on the microstructure and mechanical properties of Aermet 100 steel at the tempering temperature around 482 °C.* Journal of Alloys and Compounds, 2016. **679**: p. 184-190.

4.29 Sherby, O.D., *et al.*, *Revisiting the structure of martensite in iron-carbon steels.* Materials Transactions, 2008. **49**(9): p. 2016-2027.

4.30 Winchell, P. and M. Cohen, *The Strength of Martensite.* Trans. Quarterly, 1962. **55**: p. 347.

4.31 C Cadeville, M., J. M Friedt, and C. Lerner, *Structural, electronic and magnetic properties of splat-quenched FeCx alloys (x ⩽0.05).* Journal of Physics F: Metal Physics, 1977. **7**: p. 123.

4.32 Chakraborty, G., *et al.*, *Study on tempering behaviour of AISI 410 stainless steel.* Materials Characterization, 2015. **100**: p. 81-87.

Chapter 5: Summary and Conclusion

This chapter provides a summary of scientific knowledge obtained during this research work:

1. A cellular dendritic-like structure was observed in both as-deposited and stress relieved samples. The build-up area was predominated by martensite with 15% retained austenite. Cr and Mo segregation were detected by EDS in the region where retained austenite existed. Carbides were observed under SEM. A coarsened tempered martensitic structure close HAZ/build-up interface was observed due to multiple thermal cycles heat accumulation during the AM process. In addition, XRD results confirmed an increasing amount of $M_{23}C_6$ precipitation in the stress-relieved sample. In the heat-treated sample, the microstructure is homogenized as tempered martensite with a crystalline structure of BCC. Retained austenite has been removed after heat treatment.

2. The cooling rate has a significant impact on the tetragonality (c/a ratio) of the martensite structure. A higher cooling rate results in a higher tetragonality.

3. A comparison of hardness among as-deposited, stress-relieved and heat-treated samples revealed that the existence of $M_{23}C_6$ has significantly increased the hardness of stress-relieved sample. The stress relief treatment can be applied to PLPBF fabricated AerMet 100 since it helped to achieve a desired hardness. Heat-treated sample also exhibited a competitive hardness due to the completed martensite transformation.